

Gross Moist Stability Assessment during TOGA
COARE: Amplification and Decay of
Convection

by

KUNIAKI INOUE

A thesis submitted in partial fulfillment of the
requirements for the degree of

MASTER OF SCIENCE

(Atmospheric Sciences)

at the

UNIVERSITY OF WISCONSIN-MADISON

2014

Abstract

Daily averaged TOGA COARE data are analyzed to test our hypothesis that convection is amplified (attenuated) via sub-critical (super-critical) gross moist stability which corresponds to a bottom-heavy (top-heavy) vertical velocity profile. Gross moist stability (GMS) is a quantity which represents efficiency of moist static energy (MSE) export by convection and associated large-scale circulations. It is hypothesized that a bottom-heavy vertical velocity profile with negative GMS imports MSE efficiently and enhances the convection, and in contrast that a top-heavy profile with positive GMS exports MSE from the atmospheric column, attenuating the convection.

In order to test this hypothesis, precipitation changes and probabilities of precipitation increase are plotted as a function of the GMS. This analysis verifies that negative (positive) GMS corresponds to an increase (a decrease) in precipitation, which is consistent with the hypothesis. Furthermore, we find that values of the GMS are related to convective life-cycles, in which convection starts with a structure having high efficiency of MSE import (negative and large GMS), the MSE-import efficiency reduces as the convection develops (near neutral GMS), and eventually evolves into a structure which exports MSE from the convective system (positive GMS). In order to determine which factor regulates the efficiency of the MSE import/export, the effects of MSE advection, radiative heating and surface fluxes are examined. This investigation suggests that the efficiency of the MSE import/export is primarily regulated by variations of

vertical velocity profiles, indicating that the convective amplification/attenuation is tightly connected with the variations of the shape of the vertical velocity profiles.

A small modification of the definition of the GMS is introduced in order to investigate relationships between vertical atmospheric structures, the modified GMS, and intensity of the convection. Through the analysis, we find that a temperature inversion in the middle troposphere plays a crucial role in convective amplification. In the early stages of convection, the inversion layer in the middle troposphere behaves as a lid, preventing the convection from penetrating that layer. As a result, convection with a bottom-heavy shape cannot become a top-heavy shape, maintaining high efficiency of MSE import via low level convergence, which makes the convective system more favorable for further convection. Consequently, the convective system which stores enough MSE can evolve into intense convection.

Contents

	Abstract.....	i
	Contents.....	iii
	List of figures.....	v
	Acknowledgments.....	viii
1.	Introduction.....	1
2.	Data description.....	12
3.	Theoretical framework.....	14
	3.1 Basic equations.....	14
	3.2 Amplifying and decaying phases.....	19
	3.3 GMS and GMS-criticality.....	21
	3.4 More descriptions regarding MSE budgets.....	22
4.	Results and discussion I: GMS-criticality and convection.....	34
	4.1 GMS-criticality and amplifying or decaying phases.....	34
	4.2 GMS-criticality and life-cycles of convection.....	40
	4.3 Effects of radiative heating and surface flux.....	45
5.	Modification of theory.....	50
6.	Results and discussion II: MGMS-criticality and convection.....	53
	6.1 MGMS-criticality and amplifying or decaying phases.....	53
	6.2 Vertical structures of omega and wind divergence.....	57
	6.3 Vertical structures of anomalous DSE and moisture.....	60

6.4	MGMS-criticality and intensity of convection.....	64
7.	Conclusion.....	67
8.	Future work.....	71
9.	References.....	73

List of figures

- Figure 1 Binned daily average precipitation P in 1%-wide bins of column relative humidity r for the four tropical ocean regions, Indian Ocean, W. Pacific, E. Pacific, and Atlantic (from Bretherton et al. 2004).
- Figure 2 Ensemble average precipitation $\langle P \rangle$, conditionally averaged by 0.3-mm bins of column water vapor w for 1-K bins of the vertically averaged tropospheric temperature \hat{T} for the eastern Pacific. Lines show power-law fits above the critical point (from Neelin et al. 2009).
- Figure 3 Relationship between precipitation and column relative humidity for organized convective system. Different colored symbols correspond to different reference column relative humidity (CRH) that is column relative humidity at the convective peak. The solid black line represents the climatological pattern. Each trajectory shows a life-cycle of convection with different reference CRH. Each point is spaced at every 30 minutes over 96-hour convective life-cycle (from Masunaga 2012).
- Figure 4 Schematic figure of a typical MSE profile and two different shapes of vertical velocity (ω) profiles. Arrows represent air flows of convection and its associated large-scale circulations. Leftward (rightward) arrows correspond to convergence (divergence).
- Figure 5 Composite structure of the intensive observation period (IOP) of TOGA COARE. The large-scale domain (LSD), the outer sounding array (OSA), and the intensive flux array (IFA) are outlined. Each symbol shows the location of the station (from Webster and Lukas 1992).
- Figure 6 (a) Power spectrum of $\frac{\partial \langle s \rangle}{\partial t}$. (b) Power spectrum of $\frac{\partial \langle q \rangle}{\partial t}$. (c) Time-series of $\frac{\partial \langle s \rangle}{\partial t}$ for raw, 24-hour running mean, and 4-day running mean data during TOGA COARE. (d) Time-series of $\frac{\partial \langle q \rangle}{\partial t}$ in a unit of energy for raw, 24-hour running mean, and 4-day running mean data.
- Figure 7 Relationship between precipitation and column-integrated water vapor in the TOGA COARE data. Each variable was filtered with 24-hour running mean. The black line was determined with a nonlinear fitting.
- Figure 8 (a) Power spectra of raw precipitation (gray) and filtered precipitations with 1.5~3 day band-pass filter (blue), 3~7 day band-pass filter (red), 7~20 day band-pass filter (green) and >20 day low-pass filter (black). (b)

Response functions of Lanczos filters with different cut-off frequencies. Colors are arranged in the same way as (a). Thick solid lines represent theoretical responses, and thin dash lines represent the responses computed from the power spectrum of the precipitation. (c) Time-series of raw and filtered anomalous precipitations. The black line illustrates two MJO events during TOGA COARE.

Figure 9 (Top panels) Lag auto-correlations of filtered precipitation (solid lines) and lag correlations between filtered precipitation and filtered column-integrated MSE (dash lines) on the four different time-scales. (Bottom panels) Regression slopes of anomalies of $\partial\langle h \rangle / \partial t$ (green), $-\langle \vec{v} \cdot \nabla h \rangle$ (gray dash), $-\langle \omega \partial h / \partial p \rangle$ (black), $\langle Q_R \rangle$ (red), and SF (blue), regressed against filtered precipitation and scaled with one standard deviation of the filtered precipitation on different time-scales. The precipitation was filtered with (a) 1.5~3 day band-pass filter, (b) 3~7 day band-pass filter, (c) 7~20 day band-pass filter, and (d) >20 day low-pass filter. The error bars on the left bottom corners in (a) and (b) represent average values (among the lag time windows) of significant errors for each MSE budget term computed with 90% significant level. The numbers on the right bottom corners show estimated independent sample sizes on the different time-scales.

Figure 10 (a) Binned precipitation change as a function of GSM-criticality, averaged in 30-point-bins of GSM-criticality. (b) Binned probability of precipitation increase as a function of GSM-criticality, averaged in the same bins as (a). (c) Binned precipitation as a function of GSM-criticality, averaged in the same bins as above. (d) Binned GSM-criticality as a function of precipitation, averaged in 30-point-bins of precipitation in amplifying phase ($\Gamma - \Gamma_C < 0$). (e) As in (d), but for decaying phase ($\Gamma - \Gamma_C > 0$).

Figure 11 (a) Binned minus omega profiles for convective events ($\nabla \cdot \langle s\vec{v} \rangle > 0$), averaged in 30-point-bins of GSM-criticality in amplifying phase ($\Gamma - \Gamma_C < 0$). (b) As in (a), but for decaying phase ($\Gamma - \Gamma_C > 0$). (c) As in (a), but for non-convective events ($\nabla \cdot \langle s\vec{v} \rangle < 0$). (d) As in (b), but for non-convective events ($\nabla \cdot \langle s\vec{v} \rangle < 0$). (e) ~ (f) As in (a) ~ (d), for evolutions of MSE profile.

Figure 12 Idealized conceptualization of relation between GSM and convective evolution.

Figure 13 (Top two panels) Binned precipitation and binned omega profile, averaged in 30-point-bins with respect to GSM. (Bottom two panels) As in the top two panels, but averaged in bins of GSM-criticality.

- Figure 14 (Up left) Negative total MSE advection $\nabla \cdot \langle h\vec{v} \rangle$ as a function of negative total DSE advection $\nabla \cdot \langle s\vec{v} \rangle$. (Up right) Radiative heating plus surface flux as a function of negative total DSE advection $\nabla \cdot \langle s\vec{v} \rangle$. (Bottom left) PDF of GMS. (Bottom right) PDF of critical-GMS.
- Figure 15 As in Fig. 10, but for MGMS-criticality.
- Figure 16 (Top) Binned precipitation as a function of MGMS-criticality, averaged in 30-point-bins of MGMS-criticality. (Middle) Binned omega profiles as a function of MGMS-criticality, averaged in the same bins as the top panel. (Bottom) As in the middle panel, but for wind divergence profiles.
- Figure 17 (Top) Time-series of 4-day running averaged precipitation during TOGA COARE. (Middle) Time-height structure of 4-day running averaged omega profiles. (Bottom) Corresponding divergence structure. The black boxes and arrows emphasize lower tropospheric tilting omega profiles and upper tropospheric bimodal omega structures.
- Figure 18 (Top) Binned radiative cooling and surface flux as a function of MGMS-criticality, averaged in 30-point-bins of MGMS-criticality. (Middle) Binned DSE anomaly profiles as a function of MGMS-criticality, averaged in the same bins as the top panel. (Bottom) As in the middle panel, but for moisture anomaly profiles.
- Figure 19 Schematic figure illustrating relation between temperature inversion, omega profile, moisture convergence, and convective amplification.

Acknowledgments

I would like to thank my advisor Prof. Larissa Back for her continued support and advising. My completion of this thesis could not have been accomplished without her advising. Frequent meetings, long discussions, useful suggestions, patient efforts to enhance my productivity, all of them led me to the appropriate direction to finish this thesis.

I would like to thank Prof. Greg Tripoli and Prof. Matt Hichman for their careful reviewing and useful suggestions. I also appreciate that both of them have strongly stimulated my interest in atmospheric dynamics through daily conversations and discussions in the classes. I would also like to thank Prof. Tracey Holloway, who first let me know that there exists such an exciting academic subject, Atmospheric Sciences!!!

I would like to thank the Department of Atmospheric and Oceanic Sciences for offering the admission even though my application was submitted four months later the final deadline of the application.

Finally, I would like to express my warm thanks to my wonderful families and friends who enrich my life.

1. Introduction

The dynamics of large-scale vertical motion in the tropics is significantly different from that in the mid-latitude atmosphere. In the mid-latitudes, horizontal temperature advection plays a crucial role in large-scale vertical motion. In the tropics, in contrast, horizontal temperature gradients are negligible due to small rotational constraints caused by a weak Coriolis force. As a result, horizontal temperature advection is very weak in the tropics, which indicates that tropical vertical motion is regulated by a quite different mechanism from that in the mid-latitudes. How, then is tropical vertical motion regulated? Although there are still many uncertainties in how tropical convective dynamics work, tropical meteorologists agree that there is one big hint to that question. That hint is a significant role of tropospheric moisture in the tropical convective dynamics.

Raymond (2000) first proposed a somewhat speculative hypothesis regarding tropical precipitation. He hypothesized that tropical rainfall is primarily regulated by the saturation fraction (also known as column relative humidity) that is a ratio of column-integrated water vapor (known as precipitable water or water vapor path) to column-integrated saturation specific humidity. As more satellite data became available, this hypothesis gathered more attention. From satellite data analysis, Bretherton et al. (2004) showed that precipitation over the tropical ocean is an exponential function of column relative humidity, and that exponential relation is consistent among different tropical ocean basins (Fig. 1). Since then, different researchers have investigated the

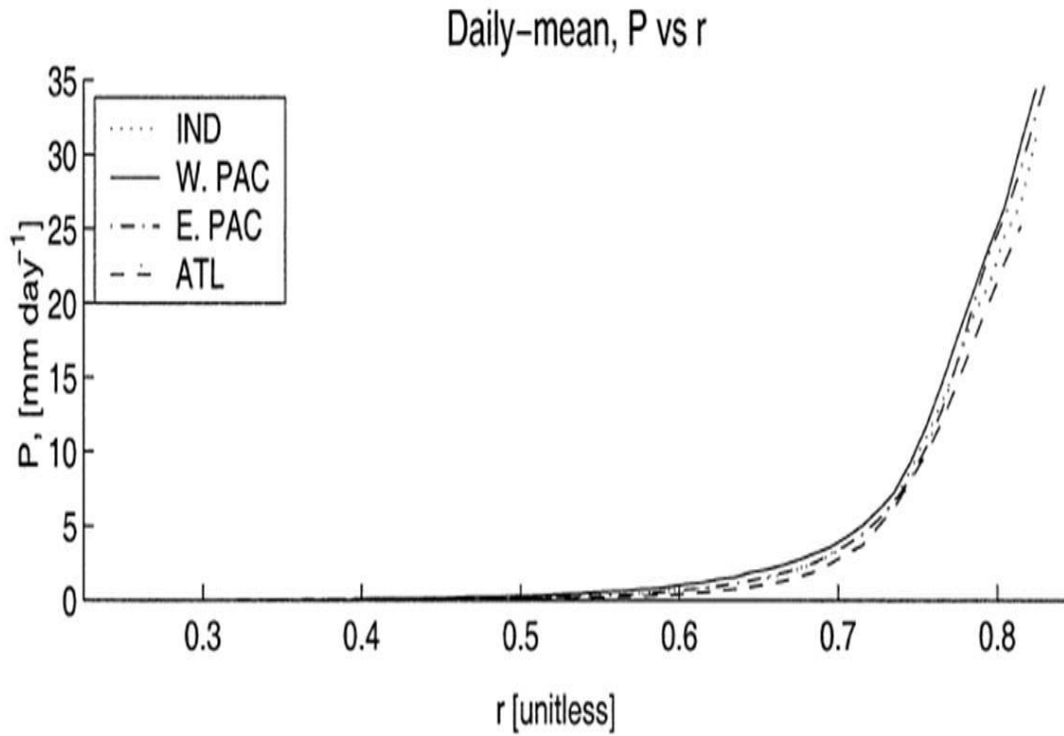


Figure 1: Binned daily average precipitation P in 1%-wide bins of column relative humidity r for the four tropical ocean regions, Indian Ocean, W. Pacific, E. Pacific, and Atlantic (from Bretherton et al. 2004).

precipitation-moisture relationship. Neelin et al. (2009) showed that precipitation as a function of column-integrated water vapor conforms to a power-law above a critical value which is determined by mean tropospheric temperature (Fig. 2). Masunaga (2012) found that the relationship between precipitation and column relative humidity on short time-scale exhibits a highly nonlinear pattern with circulating trajectories (Fig. 3). Although there are differences in details, those studies consistently suggest that there is a tight, positive and nonlinear relationship between tropical precipitation and column-integrated water vapor. This relationship plays a key role in the dynamics of tropical convection.

Besides this moisture-convection relationship, another important concept regarding the tropical convection was provided by Sobel and Bretherton (2000), who proposed a modified model framework called the weak temperature gradient approximation (WTG). Under the WTG, free tropospheric temperature is assumed to be constant and is prescribed, which allows the precipitation and vertical velocity to be prognostic variables. This approximation has, since then, gained high popularity and also been justified in the academia of the tropical meteorology. One significant benefit of the WTG becomes prominent when one considers atmospheric moist static energy (MSE) budget. The MSE is a combination of enthalpy, geopotential, and moisture in a unit of energy, which is approximately conserved in moist adiabatic processes. Under the WTG, enthalpy is constant, which means that all variations of the MSE are primarily associated with moisture variations. Therefore, variations of the column-integrated MSE are equivalent to the variations of the column-integrated water vapor. Since the column-

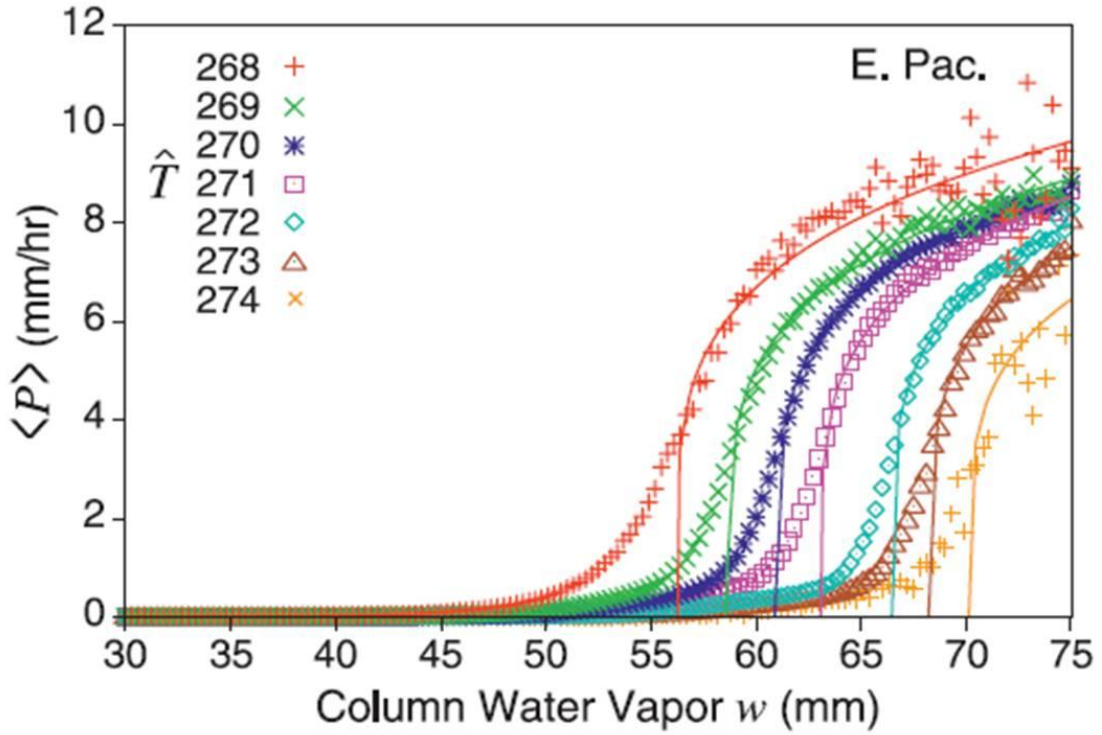


Figure 2: Ensemble average precipitation $\langle P \rangle$, conditionally averaged by 0.3-mm bins of column water vapor w for 1-K bins of the vertically averaged tropospheric temperature \hat{T} for the eastern Pacific. Lines show power-law fits above the critical point (from Neelin et al. 2009).

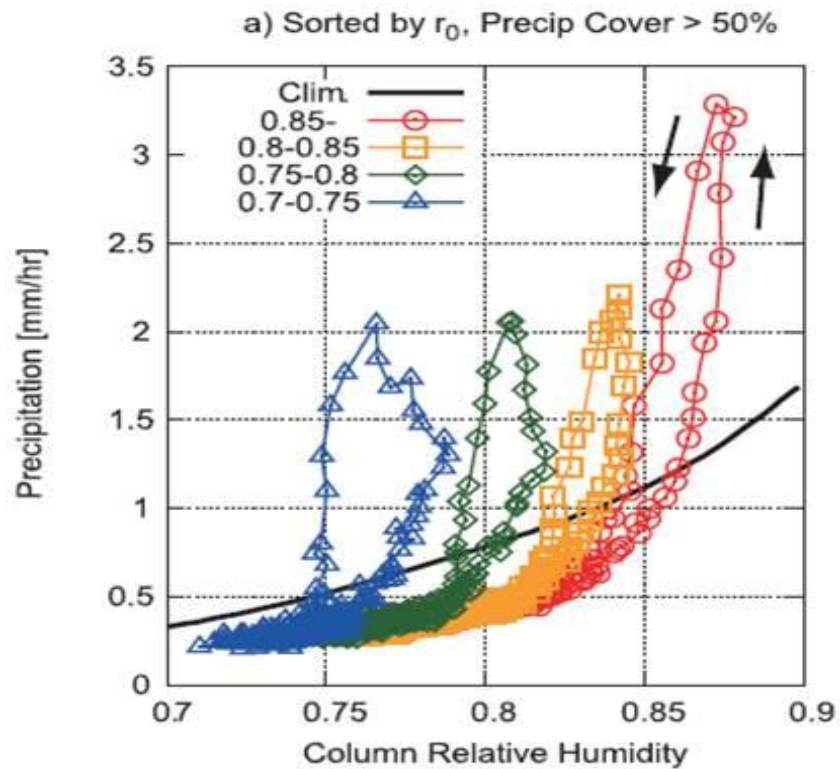


Figure 3: Relationship between precipitation and column relative humidity for organized convective system. Different colored symbols correspond to different reference column relative humidity (CRH) that is column relative humidity at the convective peak. The solid black line represents the climatological pattern. Each trajectory shows a life-cycle of convection with different reference CRH. Each point is spaced at every 30 minutes over 96-hour convective life-cycle (from Masunaga 2012).

integrated water vapor is tightly related to precipitation, we can infer that the variances of column-integrated MSE and precipitation anomalies are also tightly connected. Furthermore, by investigating the column-integrated MSE budget equation, we might be able to understand the relationships between radiative heating, surface flux, MSE advection, and precipitation.

The column-integrated MSE budget is strongly affected by vertical structures of the troposphere, especially vertical velocity profiles. Back and Bretherton (2006) pointed out that the geographical variability of omega (vertical pressure velocity) profile strongly affects the climatological MSE budget. One of the main points of their study can be summarized in a schematic figure shown in Fig. 4. In Fig. 4, the left diagram illustrates a MSE profile, and the other two diagrams represent two different shapes of vertical velocity profiles. One of them has a bottom-heavy shape, in which the peak velocity happens in the lower troposphere, while the other has a top-heavy profile which has its peak in the upper troposphere. The arrows represent large-scale circulations associated with the convection. The leftward and rightward arrows represent convergence and divergence, respectively. In the bottom-heavy shaped convection, convergence happens in the lower troposphere where the MSE is rich, and divergence happens in the middle troposphere where the MSE is poor. As a result, in this convective system, net MSE import via vertical motion happens, which increases the column-integrated MSE. In the top-heavy shaped convection, in contrast, convergence happens in the middle troposphere where the MSE is poor, and divergence happens in the upper troposphere where the MSE

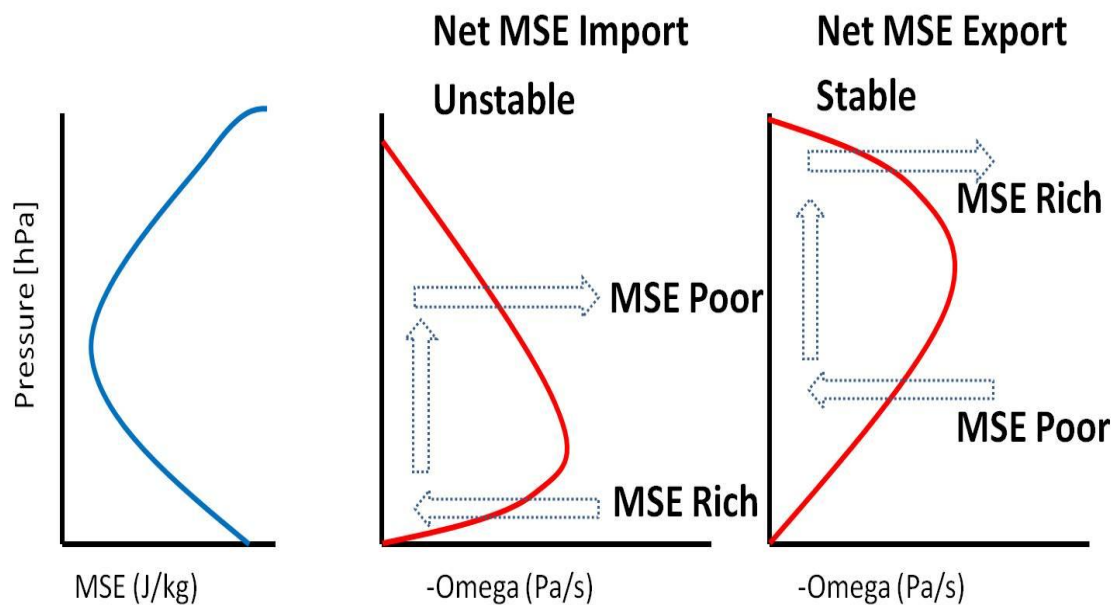


Figure 4: Schematic figure of a typical MSE profile and two different shapes of vertical velocity (ω) profiles. Arrows represent air flows of convection and its associated large-scale circulations. Leftward (rightward) arrows correspond to convergence (divergence).

is rich. As a result, in this system, net MSE export is associated with vertical motion, which decreases the column-integrated MSE in the atmospheric column.

Connecting with the column MSE-precipitation relationship discussed above, we can infer an important implication regarding the vertical velocity profile and convective stability, that is: the bottom-heavy (top-heavy) vertical velocity profile tends to increase (decrease) the column-integrated MSE, which leads to further amplification (decay) of the convection due to the moisture-convection feedback. Our main goal in this study is to systematically test whether this implication is observed in field campaign data, and if it is, then to clarify how that mechanism works.

In general, tropical convection starts with a bottom-heavy profile, which progressively deepens and eventually becomes a top-heavy profile. This transition from a bottom-heavy into a top-heavy profile can be observed in a wide range of spectrum of tropical variability, from mesoscale convective system to various kinds of convectively coupled equatorial waves to the MJO (e.g., Kikuchi and Takayabu 2004; Haertel and Kiladis 2004; Mapes et al. 2006; Peters and Bretherton 2006; Benedict and Randall 2007, Kiladis et al. 2009.) Recalling the relationship between vertical velocity profiles and convective amplification (decay) inferred above, we can connect the convective stability with convective life-cycles, more specifically with the transition of vertical velocity profiles. That is, the convection is amplified via bottom-heavy-shaped vertical velocity profiles in the beginning stage, and is attenuated via top-heavy-shaped profiles in the end stage of the convection. Some studies have stated related ideas. For instance, Stephens et al. (2004) showed that in the destabilizing stage of the convection “shallow convection

begins to increase, resulting in a steady moistening of the low levels, which plays a further role in conditioning the atmosphere for deep convection.” Kikuchi and Takayabu (2004) related this convective destabilization via lower tropospheric moistening to temperature inversions in the middle troposphere, claiming that the inversion in the middle troposphere enhances the lower tropospheric moisture convergence, thus leads to further enhancement of the convection. Although this destabilization mechanism due to the vertical velocity profile has been investigated in observational data and widely accepted, this idea was, to some extent, presented for each individual case in a case-study-wise manner because other factors, such as radiative heating and surface flux, make the dynamics complicated, and so make it challenging to generalize this idea. In this study, we want to propose a diagnostic framework on which we can test the mechanism of the convective destabilization/stabilization via bottom-heavy/top-heavy profiles. For doing that, we utilize a concept called gross moist stability (GMS).

The GMS is a concept originated by Neelin and Held (1987), which represents MSE export via convection and associated large-scale circulations. Raymond et al. (2009) furthered this concept by defining a relevant quantity called normalized GMS (NGMS). Although different authors have used slightly different definitions of the NGMS, all of them conform to one philosophy of the NGMS, which was summarized by Raymond et al. (2009), who claimed that the “gross moist stability (GMS) is the ratio of the vertically integrated horizontal divergence of some intensive quantity conserved in moist adiabatic processes and a measure of the strength of moist convection per unit area.” Following that philosophy, we used one version of the NGMS defined by

$$\Gamma = \frac{\nabla \cdot \langle h\vec{v} \rangle}{\nabla \cdot \langle s\vec{v} \rangle} \quad (1)$$

where $s \equiv C_p T + gz$ is dry static energy (DSE); $C_p T$ is enthalpy; gz is geopotential; $h \equiv s + Lq$ is moist static energy (MSE); L is the latent heat of vaporization; q is specific humidity; \vec{v} is horizontal wind velocity; ∇ is the isobaric gradient operator; and $\langle A \rangle = \left(\frac{1}{g}\right) \int_{p_S}^{p_T} A dp$ is mass-weighted column-integration. Although it should be called NGMS, we will call the quantity defined by Eq. (1) GMS in the following arguments in order to avoid confusion because we will later define a new quantity called modified GMS (MGMS). The GMS has been used in various ways. One recent popular usage is a linearization of MSE advection in MJO-toy-models (e.g., Neelin and Yu 1994; Sugiyama 2009; Sobel and Maloney 2012, 2013; the definitions of the GMS used here are slightly different from Eq. (1), but the idea is similar). Other studies have investigated the relations between the propagation speed of convectively coupled equatorial waves and GMS (e.g., Tian and Ramanathan 2003; Frierson 2007; Raymond et al. 2009 and references therein). In this study, we will use the GMS in a different way from the previous studies. We will focus on the physical interpretation of the GMS; that is, the GMS represents efficiency of MSE export by the convective system. Recalling the arguments about the MSE export and vertical velocity profiles, we can easily make a conjecture regarding the relations between the MSE export, vertical velocity profiles, convective amplification (attenuation), and the GMS.

The main purpose of this paper is to test our hypothesis that tropical convection is amplified (attenuated) by bottom-heavy-shaped (top-heavy-shaped) vertical velocity

profiles which import (export) MSE and moisten (dry) the convective system. We can rephrase this hypothesis from a perspective of the GMS. The convective system is amplified by a bottom-heavy profile via negative (or “effectively” negative) GMS, and it is stabilized by a top-heavy profile via positive (or “effectively” positive) GMS. For testing our hypothesis, we investigated field campaign data from TOGA COARE.

The rest of this thesis is organized as follows. Section 2 describes the data set we used (the TOGA COARE data set). Section 3 sets forth the theoretical framework of the relationship between the column-integrated MSE budgets and amplification or attenuation of tropical convection. In this section, we introduce a new quantity called GMS-criticality. By using the TOGA COARE data set, we examine our hypothesis in section 4. In section 5, we suggest slight modifications to the definition of the GMS and GMS-criticality, introducing modified quantities called modified GMS (MGMS) and MGMS-criticality. In section 6, we examine our hypothesis by using the MGMS and MGMS-criticality. Concluding remarks are provided in section 7.

2. Data description

We used field campaign data from the Tropical Ocean Global Atmosphere Coupled Ocean-Atmosphere Response Experiment (TOGA COARE; Webster and Lukas 1992) to clarify the relationship between the GMS, vertical atmospheric structures (especially the vertical velocity profile), and convective amplification/decay. TOGA COARE takes place in the western Pacific warm pool region. The TOGA COARE observational network consists of three spatially overlapping observational domains as shown in Fig. 5: the large-scale arrays (LSA), outer sounding arrays (OSA), and intensive flux arrays (IFA). In this study, we only analyzed the data collected over the IFA. The IFA is centered at 2° S, 156° E, bounded by the polygon defined by the meteorological stations at Kapingamarangi and Kavieng and ships located near 2° S, 158° E and 4° S, 155° E. The sounding data was collected during the 4-month Intensive Observing Period (IOP; 1 November 1992-28 February 1993) with 6 hourly time resolution.

The data set utilized for this study was constructed by Minghua Zhang, who analyzed the sounding data during TOGA COARE by using an objective scheme called constrained variational analysis (Zhang and Lin 1997). In that scheme, the state variables of the atmosphere are adjusted by the smallest possible amount to conserve column-integrated mass, moisture, static energy, and momentum. For more detailed information about that scheme, refer to Zhang and Lin (1997).

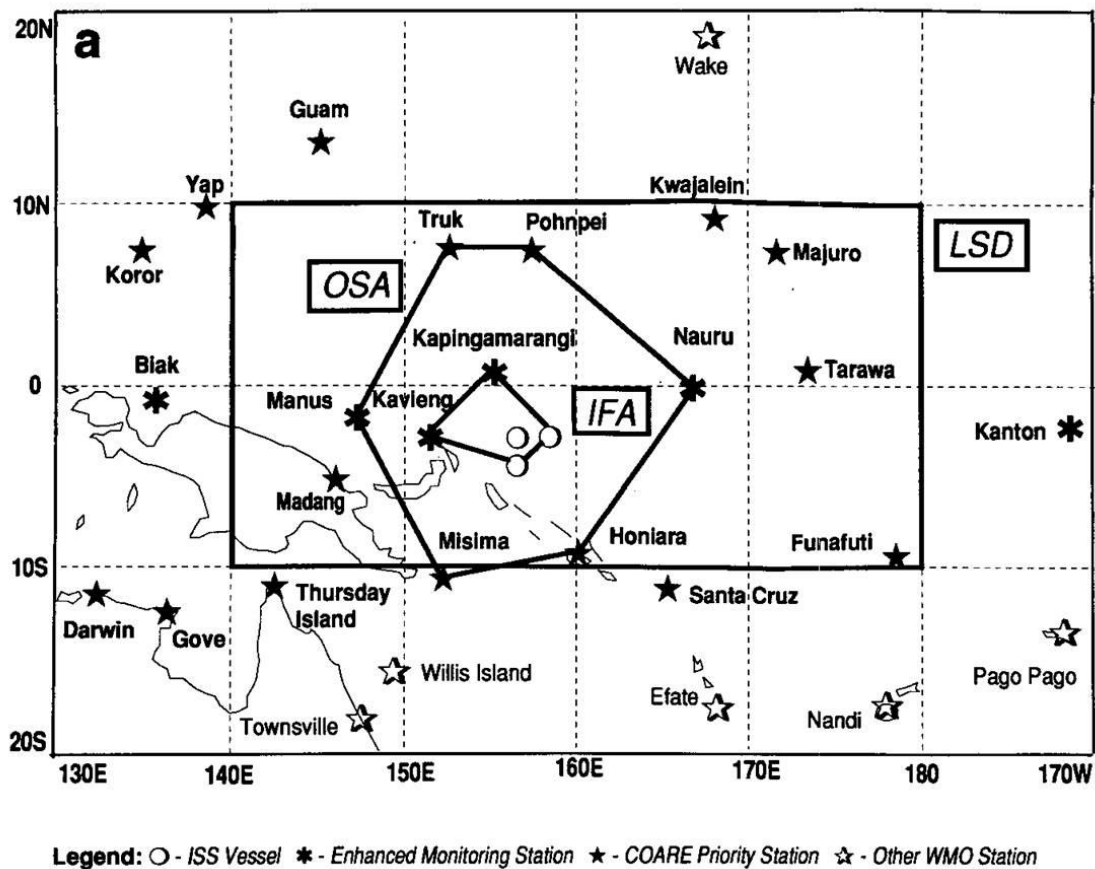


Figure 5: Composite structure of the intensive observation period (IOP) of TOGA COARE. The large-scale domain (LSD), the outer sounding array (OSA), and the intensive flux array (IFA) are outlined. Each symbol shows the location of the station (from Webster and Lukas 1992).

3. Theoretical framework

3.1 Basic equations

Following Yanai et al. (1973) and Yanai and Johnson (1993), the vertical integration of energy and moisture equations yields

$$\frac{\partial \langle s \rangle}{\partial t} + \langle \vec{v} \cdot \nabla s \rangle + \langle \omega \frac{\partial s}{\partial p} \rangle = \langle Q_R \rangle + LP + SH \quad (2)$$

$$\frac{\partial \langle Lq \rangle}{\partial t} + \langle \vec{v} \cdot \nabla Lq \rangle + \langle \omega \frac{\partial Lq}{\partial p} \rangle = LE - LP \quad (3)$$

where $s \equiv C_p T + gz$ is dry static energy (DSE); $C_p T$ is enthalpy; gz is geopotential; \vec{v} is horizontal wind velocity; ω is vertical pressure-velocity; L is the latent heat of vaporization; q is specific humidity; P is precipitation rate; SH is surface sensible heat flux; Q_R is radiative heating rate; E is surface evaporation; ∇ is the isobaric gradient operator; and $\langle A \rangle = \left(\frac{1}{g} \right) \int_{P_S}^{P_T} A dp$ is mass-weighted column-integration from the surface pressure (1000 hPa) to the tropopause pressure (100 hPa). Each quantity is averaged over the IFA. In deriving these equations, we employ the continuity equation $\nabla \cdot \vec{v} + \frac{\partial \omega}{\partial p} = 0$, and neglect divergence of kinetic energy, which is generally small in the tropics. We further assume that $\omega = 0$ at the surface and tropopause pressure, and take integration by parts to obtain

$$\frac{\partial \langle s \rangle}{\partial t} + \nabla \cdot \langle s \vec{v} \rangle = \langle Q_R \rangle + LP + SH \quad (4)$$

$$\frac{\partial \langle Lq \rangle}{\partial t} + \nabla \cdot \langle Lq \vec{v} \rangle = LE - LP . \quad (5)$$

In the deep tropics, a temperature profile (or DSE profile) is relatively constant in time and horizontal spaces primarily because rotational constraints due to the Coriolis force are so weak that buoyancy anomalies created in clouds are quickly spread out and eliminated in the adjustment mechanism of gravity waves (Charney 1963, 1969; Bretherton and Smolarkiewicz 1989). Based on these ideas, Sobel and Bretherton (2000) proposed the weak temperature gradient approximation in which the free tropospheric temperature profile over the tropics is set to be constant so that temperature tendency and horizontal temperature advection disappear from the temperature equation. (Since we assume that the pressure field is in the hydrostatic balance, there is no geopotential tendency; that is $\frac{\partial \langle s \rangle}{\partial t} = C_P \frac{\partial \langle T \rangle}{\partial t} \cong 0$.) This weak temperature gradient approximation has been widely accepted within the academia of the tropical meteorology as a basic model framework for understanding tropical convection. Based on that approximation, we assume that the tendency and horizontal advective terms in Eq. (4) are negligible.

A primary exception to this assumption is a diurnal cycle of temperature field. Generally, free tropospheric temperature varies significantly due to a diurnal oscillation of the solar radiation, and thus the DSE tendency term in Eq. (4) cannot be neglected in a short time-scale.

Figure 6 shows that that assumption is valid if the diurnal cycle of the tendency term is removed. Figure 6a illustrates that most of the variances of the column DSE tendency are explained solely by the diurnal cycle. Thus a time filter with a time window longer than 24 hours enables us to exclude the column-integrated DSE tendency term

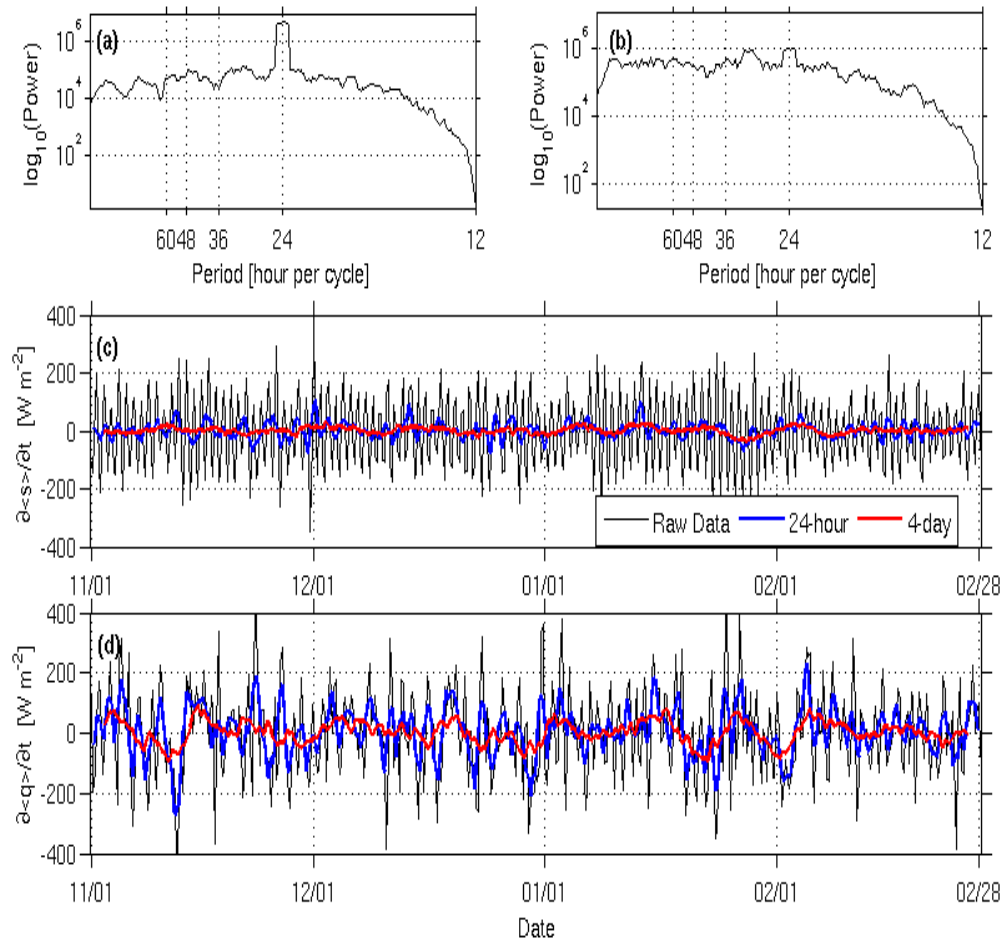


Figure 6: (a) Power spectrum of $\frac{\partial\langle s \rangle}{\partial t}$. (b) Power spectrum of $\frac{\partial\langle q \rangle}{\partial t}$. (c) Time-series of $\frac{\partial\langle s \rangle}{\partial t}$ for raw, 24-hour running mean, and 4-day running mean data during TOGA COARE. (d) Time-series of $\frac{\partial\langle q \rangle}{\partial t}$ in a unit of energy for raw, 24-hour running mean, and 4-day running mean data.

from Eq. (4). Figure 6c shows the time series of the raw and time-filtered $\frac{\partial \langle s \rangle}{\partial t}$. Running mean filters whose time windows are longer than 24 hours yield much smaller variances than those of the raw data, making the column DSE tendency negligible.

In contrast, Figs. 6b and 6d show that the column-integrated moisture tendency varies significantly even after taking the running mean filters. This fact has been pointed out by Mapes et al. (2006), who suggested that the ratio of water vapor anomalies to temperature anomalies becomes larger for longer time-scale variability, implying that moisture anomalies play a more important role than temperature anomalies do in the dynamics of large-scale tropical convection.

We want to note that although $\frac{\partial \langle s \rangle}{\partial t}$ can be ignored when vertically integrated and compared to the other terms in Eqs. (4) and (5), it is not completely zero, and small local variations of $\frac{\partial s}{\partial t}$ (particularly its vertical profile) may play a significant role in local dynamics of moist convection, which will be described in more detail in section 6.

Although we will not show the figures, the horizontal DSE advection is much smaller than the other terms in Eqs. (4) and (5). Thus we can, with no doubt, ignore the horizontal DSE advection. The horizontal moisture advection, in contrast, varies significantly, implying the horizontal moisture advection is an important factor in the dynamics of tropical convection.

Applying the time filter and the weak temperature gradient approximation to Eqs. (4) and (5) yields

$$\nabla \cdot \langle s \vec{v} \rangle^* = \langle Q_R \rangle^* + LP^* + SH^* \quad (6)$$

$$\frac{\partial \langle Lq \rangle^*}{\partial t} + \nabla \cdot \langle Lq \vec{v} \rangle^* = LE^* - LP^* \quad (7)$$

where the star-mark represents time filters whose time windows are longer than 24 hours. (Strictly speaking, the horizontal DSE advection should be removed from Eq. (6) so that $\nabla \cdot \langle s \vec{v} \rangle^* \cong \langle \omega \frac{\partial s}{\partial p} \rangle^*$. We will keep using the flux form of the DSE advection like Eq. (6) in the following arguments just for convenience. One can consider in the following arguments that $\nabla \cdot \langle s \vec{v} \rangle^* \cong \langle \omega \frac{\partial s}{\partial p} \rangle^*$.) By adding Eqs. (6) and (7), we obtain

$$\frac{\partial \langle Lq \rangle^*}{\partial t} + \nabla \cdot \langle h \vec{v} \rangle^* = \langle Q_R \rangle^* + SF^* \quad (8)$$

where $h \equiv s + Lq$ is moist static energy (MSE) and $SF \equiv LE + SH$ is surface flux. In the following discussions, the star-marks will be dropped, but all the variables below represent time-filtered ones unless remarks are given.

As a next step, we utilize a relationship between precipitation and column-integrated water vapor. Bretherton et al. (2004) have shown a tight relationship between precipitation and column relative humidity r , which is calculated by $r = \langle q \rangle / \langle q_s \rangle$ where q_s is saturation specific humidity and $\langle \ \rangle$ is vertical integration. Using the satellite data, they have shown that the relationship is in the form, $P = \exp[\tilde{\alpha}(r - \tilde{\beta})]$, where $\tilde{\alpha}$ and $\tilde{\beta}$ are some constants determined by a nonlinear fitting (Fig. 1). Since we assume that the temperature is relatively constant, so is $\langle q_s \rangle$ since it is a function of a temperature. Therefore, we can obtain the relationship between precipitation and $\langle q \rangle$ in the form of

$$P = \exp[\alpha(\langle q \rangle - \beta)]. \quad (9)$$

Figure 7 shows the relationship between precipitation and column-integrated water vapor in the TOGA COARE data. Each variable is daily averaged. The fitting line is determined by a nonlinear least square method. This figure shows that the proposed exponential relationship is relatively robust in the TOGA COARE data.

Taking the natural logarithm on Eq. (9) and plugging it into Eq. (8) yields

$$\frac{L}{\alpha} \frac{\partial \ln P}{\partial t} = -\nabla \cdot \langle h\vec{v} \rangle + \langle Q_R \rangle + SF. \quad (10)$$

This equation simply states that precipitation is an exponential function of moisture recharge, more specifically, a gap between sink due to precipitation and source due to moisture convergence plus evaporation (since the rhs of Eq. (10) is, under the weak temperature gradient approximation, equal to $\frac{\partial \langle Lq \rangle}{\partial t} = LE - LP - \nabla \cdot \langle Lq\vec{v} \rangle$ according to the moisture budget equation Eq. (7).) By investigating the rhs of Eq. (10), we can diagnose relative contributions of the MSE advection, radiative heating, and surface flux to the moisture recharge, thus to the rate of the change of precipitation.

3.2 Amplifying and decaying phases

Equation (10) indicates two moist convective phases:

$$\nabla \cdot \langle h\vec{v} \rangle - F < 0 \quad (\text{p.1a})$$

$$\nabla \cdot \langle h\vec{v} \rangle - F > 0 \quad (\text{p.2a})$$

where $F \equiv \langle Q_R \rangle + SF$. According to Eq. (10), precipitation will increase over time if a system is in (p.1a), and precipitation will decrease if a system is in (p.2a). In the phase (p.1a), MSE gains by the advection and the surface flux exceed the dissipation by the

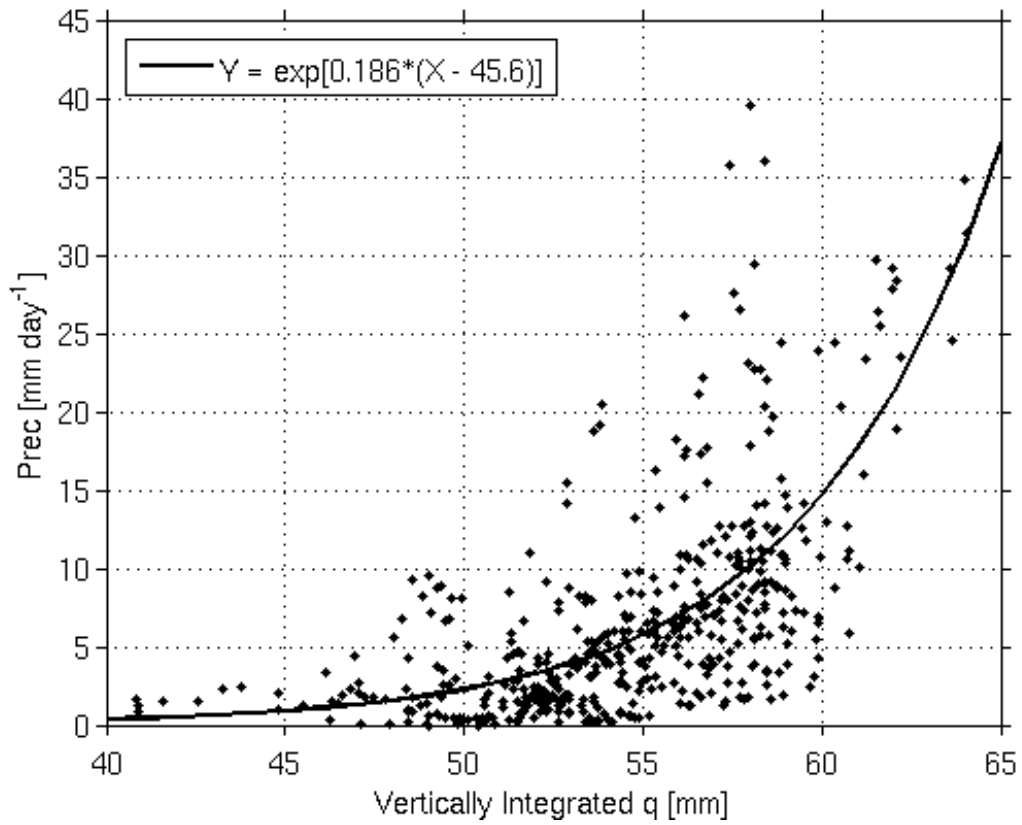


Figure 7: Relationship between precipitation and column-integrated water vapor in the TOGA COARE data. Each variable was filtered with 24-hour running mean. The black line was determined with a nonlinear fitting.

radiative cooling, causing the system to be moistened which is a favorable condition for moist convection, leading to further enhancement of the convection. Conversely, in the phase (p.2a), the advection and the radiative cooling discharge more MSE than the gain via the surface flux, which makes the convection decay over time. More thorough explanations regarding criteria (p.1a) and (p.2a) will be given later.

3.3 GMS and GMS-criticality

Since the amount of variances of the moisture discharge, $\nabla \cdot \langle h\vec{v} \rangle - F$, is dependent on the intensity of the convection, it would be advantageous to normalize it by the intensity of the convection so that we can take composites of all the convective events with different intensities in the TOGA COARE data. If we only consider situations when $\nabla \cdot \langle s\vec{v} \rangle$ is positive (this corresponds to situations when convection is active and DSE is being exported), dividing both sides of (p.1a) and (p.2a) by $\nabla \cdot \langle s\vec{v} \rangle$ yields

$$\Gamma - \Gamma_C < 0 \quad (\text{p.1b})$$

$$\Gamma - \Gamma_C > 0 \quad (\text{p.2b})$$

where Γ is the GMS defined by Eq. (1), $\Gamma_C \equiv \frac{\langle Q_R \rangle + SF}{\nabla \cdot \langle s\vec{v} \rangle}$ which we name critical-GMS, and we call the quantity, $\Gamma - \Gamma_C$, GMS-criticality. This GMS-criticality is analogous to the concept of effective GMS (e.g., Hannah and Maloney 2014). If the GMS-criticality is negative (Phase (p.1b): some studies call this condition effectively negative GMS) the system is in the amplifying phase, which augments the moist convection. Conversely, if the GMS-criticality is positive (Phase (p.2b): or effectively positive GMS) the system is in the decaying phase, leading to attenuation of the moist convection. When $\nabla \cdot \langle s\vec{v} \rangle$ is

negative, those relations are reversed, that is, (p.1b) and (p.2b) represent decaying and amplifying phases, respectively. But that case is of less importance because negative $\nabla \cdot \langle s\vec{v} \rangle$ (or DSE import) usually corresponds to non-convective events in which downward motion is dominant over the troposphere. More details will be described in section 4.

3.4 More descriptions regarding MSE budgets

It is desirable to interpret the physical meaning of the criteria (p.1a) and (p.2a) more thoroughly. For doing that, the MSE budget equation is analyzed carefully. The MSE budget equation is defined as

$$\frac{\partial \langle h \rangle}{\partial t} + \langle \vec{v} \cdot \nabla h \rangle + \langle \omega \frac{\partial h}{\partial p} \rangle = \langle Q_R \rangle + SF. \quad (11)$$

Under the weak temperature gradient approximation, Eq. (11) becomes equivalent to Eq. (8).

Since the TOGA COARE data includes a wide spectrum of tropical variability from mesoscale convective systems with time-scale a few days to convectively coupled equatorial waves (2~15 day scale) to two MJO events (30~ 60 day scale), in order to draw conclusions regarding the MSE budget behaviors each time-scale has to be separately investigated. This task was done by using a band-pass filter. More specifically, for separating different time-scales we employed Lanczos filter (Duchon 1976). We will leave detailed descriptions regarding properties and usage of that filter for my PhD thesis. Lanczos filter was applied only for Fig. 8 and Fig. 9, and in the other figures we utilized simple running mean filters.

We chose four different time-scales, 1.5~3 day, 3~7 day, 7~20 day, and >20 day (MJO) scales based on the power spectrum of the precipitation (Fig. 8a) during TOGA COARE. Those choices are also justified by past TOGA COARE studies (e.g., Takayabu et al. 1996; Haertel and Kiladis 2004; Yanai et al. 2000; Valden and Young 1997.) Figure 8b illustrates the response function of the band-pass filters, and Fig. 8c shows raw and filtered time-series of the precipitation during TOGA COARE. Using those band-pass filters, the MSE budgets in the TOGA COARE data were investigated on the four different time-scales.

Figure 9 illustrates behaviors of the MSE budgets on the four different time-scales. In the top panels, plotted are auto-correlations of precipitation, correlations between precipitation and column-integrated MSE, and in the bottom panels, plotted are regression slopes of each term in Eq. (11) regressed against the filtered precipitation and scaled with one standard deviation of the filtered precipitation on the different time-scales. Significant errors of the regression slopes with 90% significant level are also plotted on the left bottom corners only for 1.5~3 day and 3~7 day scales on which we can get enough degrees of freedom. Since this figure contains too much information, we want to summarize only a couple results which are most relevant to this thesis.

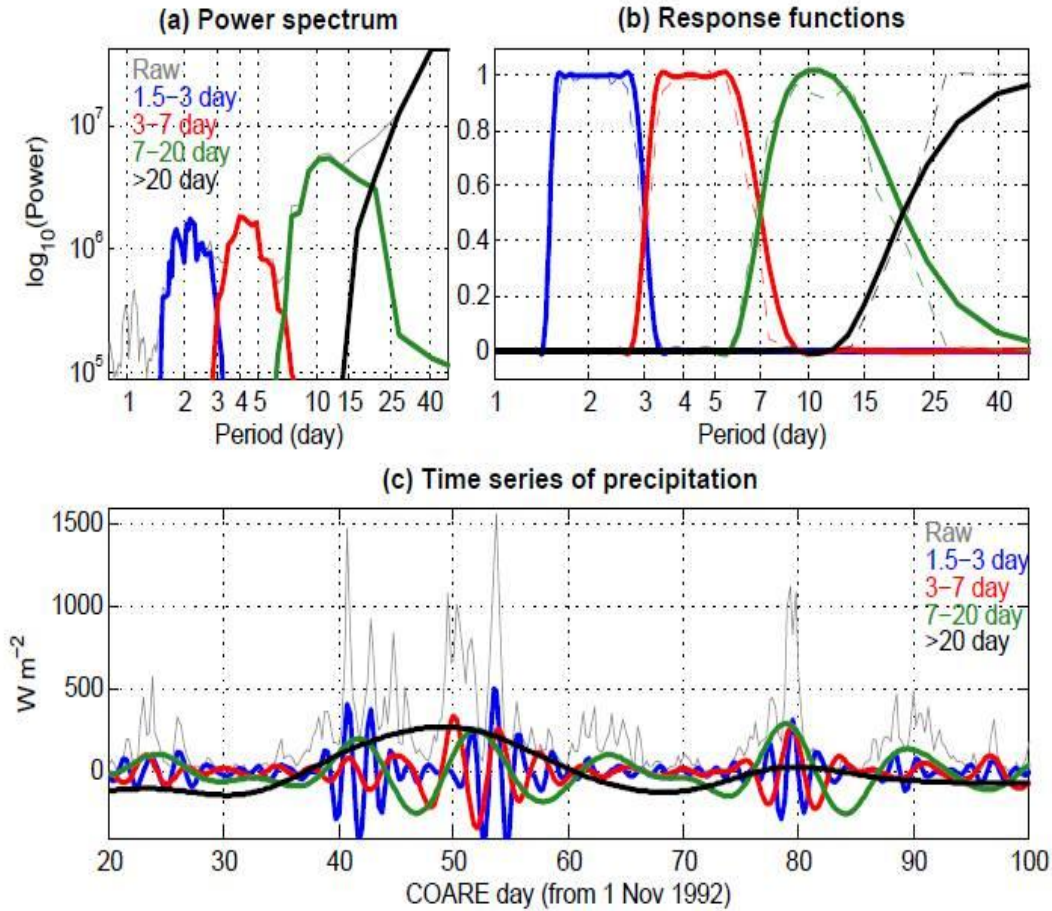


Figure 8:(a) Power spectra of raw precipitation (gray) and filtered precipitations with 1.5~3 day band-pass filter (blue), 3~7 day band-pass filter (red), 7~20 day band-pass filter (green) and >20 day low-pass filter (black). (b) Response functions of Lanczos filters with different cut-off frequencies. Colors are arranged in the same way as (a). Thick solid lines represent theoretical responses, and thin dash lines represent the responses computed from the power spectrum of the precipitation. (c) Time-series of raw and filtered anomalous precipitations. The black line illustrates two MJO events during TOGA COARE.

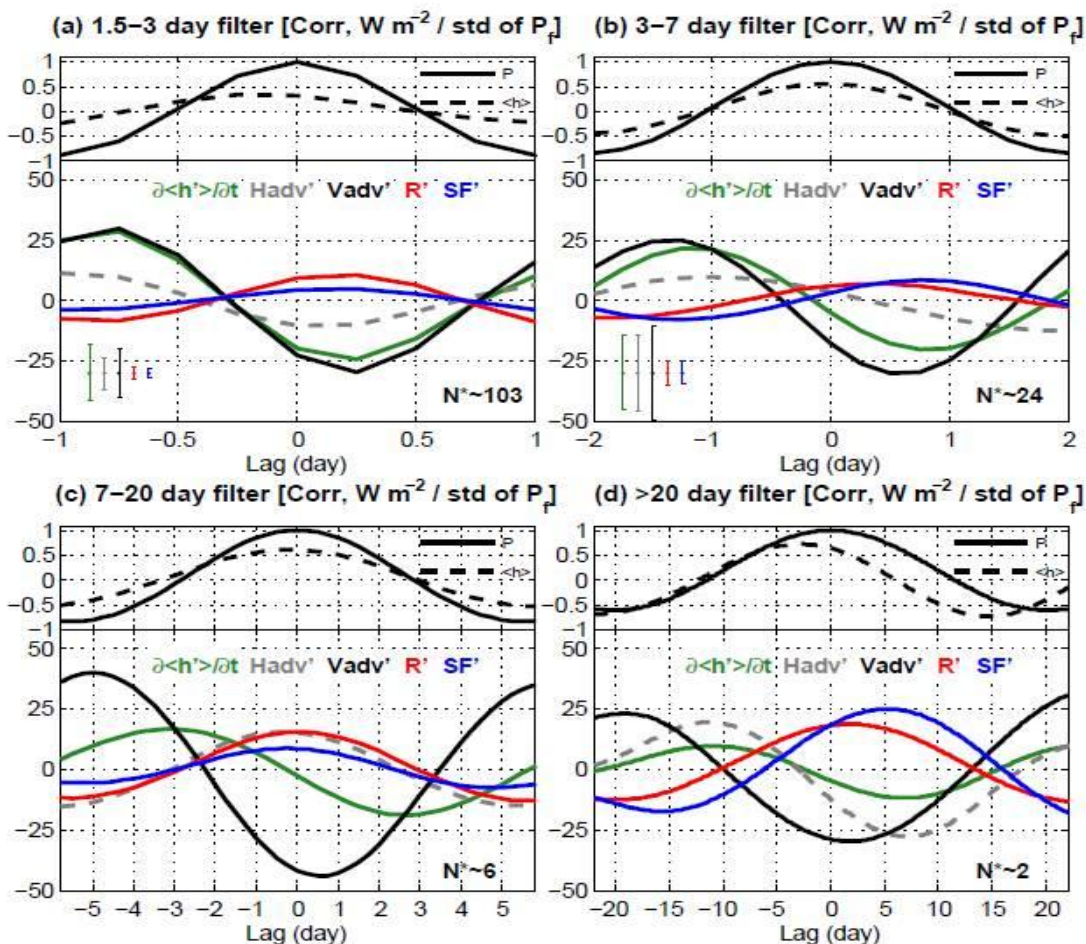


Figure 9: (Top panels) Lag auto-correlations of filtered precipitation (solid lines) and lag correlations between filtered precipitation and filtered column-integrated MSE (dash lines) on the four different time-scales. (Bottom panels) Regression slopes of anomalies of $\partial\langle h' \rangle / \partial t$ (green), $-\langle \vec{v}' \cdot \nabla h' \rangle$ (gray dash), $-\langle \omega' \partial h' / \partial p' \rangle$ (black), $\langle Q_R' \rangle$ (red), and SF' (blue), regressed against filtered precipitation and scaled with one standard deviation of the filtered precipitation on different time-scales. The precipitation was filtered with (a) 1.5~3 day band-pass filter, (b) 3~7 day band-pass filter, (c) 7~20 day band-pass filter, and (d) >20 day low-pass filter. The error bars on the left bottom corners in (a) and (b) represent average values (among the lag time windows) of significant errors for each MSE budget term computed with 90% significant level. The numbers on the right bottom corners show estimated independent sample sizes on the different time-scales.

We can summarize the results as followings:

1. On the shorter time-scales (1.5~3 day and 3~7 day scales), vertical advection, $-\langle \omega \frac{\partial h}{\partial p} \rangle$, accounts for most of the MSE recharge, $\frac{\partial \langle h \rangle}{\partial t}$, and the other terms cancel out each other so that $\frac{\partial \langle h \rangle}{\partial t} \cong -\langle \omega \frac{\partial h}{\partial p} \rangle$.
2. On all the time-scales except for the MJO scale (>20 day), the vertical advection is the most dominant process with the greatest magnitude of variances.
3. As the time-scale gets longer, relative contributions of the other terms than the vertical advection become greater. Especially on the MJO scale, all the terms (horizontal advection, vertical advection, radiative heating, and surface flux) have approximately the same magnitude of variances.
4. Horizontal advection behaves differently on the different time-scales.
5. Behavior of the radiative heating and of the surface flux are relatively consistent among the different time-scales. The maximum radiative heating and surface flux slightly lag the precipitation peak.

The above results suggest that the criteria (p.1a) and (p.2a) have different implications on different time-scales. Let's look at each budget term more closely.

As discussed above, the vertical advection is the most dominant process with the maximum magnitude of variances on all the time-scales except for the MJO scale. We examined the vertical structures of the vertical advection (not shown here) on the different time-scales, and found that the structural properties are relatively consistent among all the time-scales (except for the MJO scale). Those properties are similar to the behaviors depicted in the schematic, Fig. 4. In the beginning stage of convection, a

bottom-heavy-shaped vertical velocity profile imports MSE from lower troposphere via convergence at low levels, which is followed by a top-heavy-shaped profile in the mature stage of convection which exports MSE from the upper troposphere via upper tropospheric divergence. Therefore, the vertical MSE advection itself behaves like a self-regulating system, in which the vertical velocity profile transforms from a bottom-heavy into a top-heavy shape, and consequently the system changes itself from MSE-importing into MSE-exporting phases in the convective life-cycle. As the time-scale gets longer, the bottom-heaviness becomes less significant, and consequently, in the MJO scale the MSE import via bottom-heaviness becomes much weaker than those on the shorter time-scales.

The radiative heating has a significant positive correlation with the precipitation (correlation coefficient is ~ 0.8) among all the time-scales. This pattern can be explained from a perspective of cloudiness. As the convection develops, the cloudiness and cloud top height increase, causing a decrease in the longwave radiation which escapes from the atmosphere into space, which decreases the radiative cooling (i.e., radiative heating becomes less negative). Eventually, the cloudiness starts to decrease due to the precipitation, causing increase in the radiative cooling (i.e. more negative radiative heating), going back to the suppression stage of the convection. These transitions of decrease and increase in the radiative cooling are linear with respect to the amount of the precipitation in the TOGA COARE data, causing a high value of the correlation coefficient. Therefore, the radiative heating can be considered as an intrinsic property of the convection. (By using the phrase “intrinsic property of convection”, we mean that the

property is primarily regulated by the convective system, and not by the background conditions.)

The surface flux is more complicated than the two budget terms described above. Generally, surface flux has a positive correlation with precipitation, but it is not so high (the correlation coefficient is ~ 0.5 in the TOGA COARE data). The amount of the surface flux is computed with a bulk formula which is determined by surface wind, SST, surface air temperature, surface air specific humidity, and exchange coefficients which are affected by static stability, surface wind speeds, surface properties, and so on (Fairall et al. 2003). Some of those variables are intrinsic properties of convective systems. For instance, some portions of surface wind patterns are determined by Matsuno-Gill type model of equatorial wave dynamics (Matsuno 1966; Gill 1980). The maximum surface flux slightly lags the precipitation peak, potentially due to gustiness caused by downdrafts in deep convection which is correlated with the convection, but is highly nonlinear. (In the bulk formula used in the TOGA COARE data, the gustiness was represented as boundary layer-scale eddies; Fairall et al. 2003). Some components in the bulk formula are extrinsic properties of the convective system. For instance, the surface flux is affected by background surface wind which might not be correlated to the convective system (maybe rotational components of horizontal winds). Dry or moist intrusions due to environmental horizontal moisture gradient may also play a role in determining the surface moisture, and thus the surface flux. Therefore, the surface flux is regulated by both intrinsic and extrinsic properties of convection and by both linear and nonlinear dynamics, causing a moderate positive correlation with precipitation, and thus

we cannot consider the surface flux as a simple self-regulating system in the convective life-cycle.

The last budget term we should consider is the horizontal MSE advection. Since horizontal DSE advection is negligible, the horizontal MSE advection is almost equivalent to horizontal moisture advection. This term is the most uncertain and might be one of the most interesting research topics which researchers, especially those who study MJO dynamics, are still trying to understand. First, we should acknowledge that we are still uncertain about how to deal with this term. But we obtained some interesting results in the TOGA COARE data set, thus we want to propose physical interpretations regarding that term.

We examined vertical structures of the horizontal advective term on the four different time-scales (not shown here), and found that on the short time-scales (1.5~3 day and 3~7 day scales) the correlations between the horizontal advection and precipitation are quite low. Statistical correlation tests were applied to test whether or not the horizontal advection is correlated with the convection, and those tests indicate that we cannot reject the null hypothesis that the correlation between horizontal advection and precipitation is zero. We applied the same statistical tests for different quantities such as vertical velocity, vertical MSE advection, zonal winds, and so on, and found that there are statistically significant correlations between those quantities and the precipitation. We also examined nonlinear relations between the horizontal advection and precipitation, and observed there was no nonlinear relation between those, either.

Those results might indicate that the horizontal MSE advection is almost completely an extrinsic property which is solely regulated by environmental conditions and is almost purely random with respect to the conditions of the convective system. This means that although the horizontal MSE advection can modulate the convective system, the convective system cannot affect the horizontal advection pattern. This might make sense if one imagines a convective system with 50~100 km scale. On the frequencies we are looking at, some portions of the horizontal winds are intrinsic properties of the convective system, but not all of those are intrinsic. Furthermore, the horizontal MSE advection is predominantly affected by the horizontal moisture gradient, which is determined by large-scale moisture distribution along the periphery and outside of the convective system. Therefore, the horizontal MSE advection is primarily regulated by environmental conditions outside of the convective system.

On longer time-scales (7~20 day and MJO scales; that implies large spatial scales), contrarily, the horizontal MSE advection possesses more robust structures than on the shorter time-scales (1.5~3 day and 3~7 day scales). Due to the lack of degrees of freedom, we could not apply rigorous statistical tests on those longer time scales using the TOGA COARE data, but regression slope analyses applied on those time-scales imply that the correlation between the horizontal MSE advection and precipitation might be larger than those on the shorter time-scales. This result might be supported by some MJO studies which pointed out a crucial role of horizontal MSE advection in MJO dynamics (e.g., Pritchard and Bretherton 2013; Sobel and Maloney 2013).

Based on the arguments above, let's look back the criteria (p.1a) and (p.2a). The criteria (p.1a) and (p.2a) can be rearranged and written as

$$\langle \omega \frac{\partial h}{\partial p} \rangle - \langle Q_R \rangle - SF < -\langle \vec{v} \cdot \nabla Lq \rangle \quad (\text{p.1c})$$

$$\langle \omega \frac{\partial h}{\partial p} \rangle - \langle Q_R \rangle - SF > -\langle \vec{v} \cdot \nabla Lq \rangle. \quad (\text{p.2c})$$

Those inequalities are arranged in such a way that the lhs of the inequality represents intrinsic components of convective systems and the rhs represents an extrinsic component of the convection. The horizontal DSE advection is neglected under the weak temperature gradient approximation. Although the surface flux contains both intrinsic and extrinsic perspectives, we arrange that term in the lhs.

In order to comprehend physical implications of the criteria (p.1c) and (p.2c), let's imagine a few different scenarios. In the first scenario, let's imagine a case when there is no horizontal moisture advection (the rhs is zero). If a small perturbation (for instance, high SST anomaly or boundary layer turbulence) initializes convection and if that convection evolves into shallow convection, then the vertical advection starts to import MSE via bottom-heavy-shaped vertical velocity, causing the lhs to be more negative and thus enhancing the convection. As the convection grows, the radiative heating becomes less negative (or the radiative cooling reduces) and surface flux becomes greater since they have positive correlations to the intensity of the convection, making the lhs further negative. Therefore, in this phase, the convection is in a positive feedback in which growth of the convection leads to further amplification via making the lhs of (p.1c) more negative.

This system eventually starts to export MSE via top-heavy-shaped vertical velocity, making the lhs greater (or less negative). However, the peaks of the radiative heating and surface flux lag the peak of the convection, and thus the radiative heating and surface flux keep increasing, making the lhs smaller (or more negative). In this stage, therefore, the vertical advection stabilizes the system via MSE export while the radiative heating and surface flux keep destabilizing the system, extending the duration of the amplifying phase. This might indicate that lag time between the peak of the precipitation and the peaks of the radiative heating and surface flux determine the length of the amplifying phase, thus the intensity of the convection in the mature stage (particularly strength of MJO in simulations).

After passing the peaks of the radiative heating and surface flux, these start to decrease while the vertical advection keep increasing (getting more positive), and eventually the radiative heating and surface flux are exceeded by the vertical advection making the lhs positive, which attenuates the convection.

Therefore, in a case when there is no horizontal moisture advection, the whole convective system behaves as a semi-self-regulating system in which the convection is enhanced or attenuated in the feedback mechanism. This system is not a pure self-regulating system primarily due to the surface flux which includes extrinsic perspectives regarding the self-regulating dynamics.

Now we want to consider a case when the horizontal MSE (moisture) advection is nonzero. If shallow convection has already happened in the system, the phase should be in the amplifying phase. Let's imagine a case when a sudden dry intrusion happens during

the amplifying phase. In such a case, although the semi-self-regulating systems in the lhs (the vertical advection, radiative heating, and surface flux) import MSE making the lhs more negative, negative horizontal moisture advection causes the rhs to be negative. If that dry intrusion is strong enough to make the rhs more negative than the lhs, the system which had been in the amplifying phase (p.1c) suddenly becomes the decaying phase (p.2c), preventing further amplification. In a similar manner, positive horizontal moisture advection (moist intrusion) can change the system which had been in the decaying phase (p.2c) into an unstable condition (p.1c), causing the system to be re-amplified.

The horizontal MSE advection can be, therefore, considered as environmental favorability for moist convection. Even if the convective system itself is favorable for further convection, the convection can decay in an environmental condition with less favorability for moist convection, which is primarily determined by horizontal moisture advection.

On longer time-scales, in contrast, the horizontal advection could be a partially self-regulating system. If that is true, then the criteria (p.1c) and (p.2c) become, to some extent, a self-regulating system. In such a case, we might be able to call (p.1c) and (p.2c) the self-amplifying phase and self-decaying phase, respectively.

Since we are still unsure about how to deal with the horizontal advective term, we combine that term with the vertical advective term, dealing with that combination as a column-integrated MSE flux, $\nabla \cdot \langle h\vec{v} \rangle$. One might be able to consider the horizontal advection included in $\nabla \cdot \langle h\vec{v} \rangle$ as random noise which is uncorrelated to convective life-cycles, at least, on short time-scale.

4. Results and discussion I: GMS-criticality and convection

4.1 GMS-criticality and amplifying or decaying phases

Investigated are the ideas of self-amplifying and self-decaying phases from the perspective of the GMS, (p.1b) and (p.2b). When computing the GMS and critical-GMS, as suggested by Raymond et al. (2009), we first take time means of the numerator and the denominator, and then take a ratio between them because that is the most natural way to compute the GMS and critical-GMS. All the events whose $|\nabla \cdot \langle s\vec{v} \rangle|$ is less than 0.5 W m^{-2} are excluded in order to avoid division by zero.

In this analysis, we used a binning method. The bins are constructed with respect to the variable in the x-axis in each figure. First, we rearrange the order of the data array of the x-axis's variable in an increasing order. The data array of the variable in the y-axis is also reordered so that the corresponding x-axis's values are aligned in an increasing order. We divide the reordered data array into bins so that each bin contains 30 consecutive points, and take averages within those bins. Finally, we plot the binned y-axis's values as a function of the binned x-axis's values.

We test whether/how often the GMS-criticality corresponds to growth/decay of precipitation anomalies as predicted in section 3. To do this, we examine precipitation change as a function of GMS-criticality and the probability of precipitation increase as a function of GMS-criticality.

Figure 10 consists of five panels. Figure 10a shows binned precipitation changes versus corresponding binned GMS criticality, $\Gamma - \Gamma_C$, only for the events in which

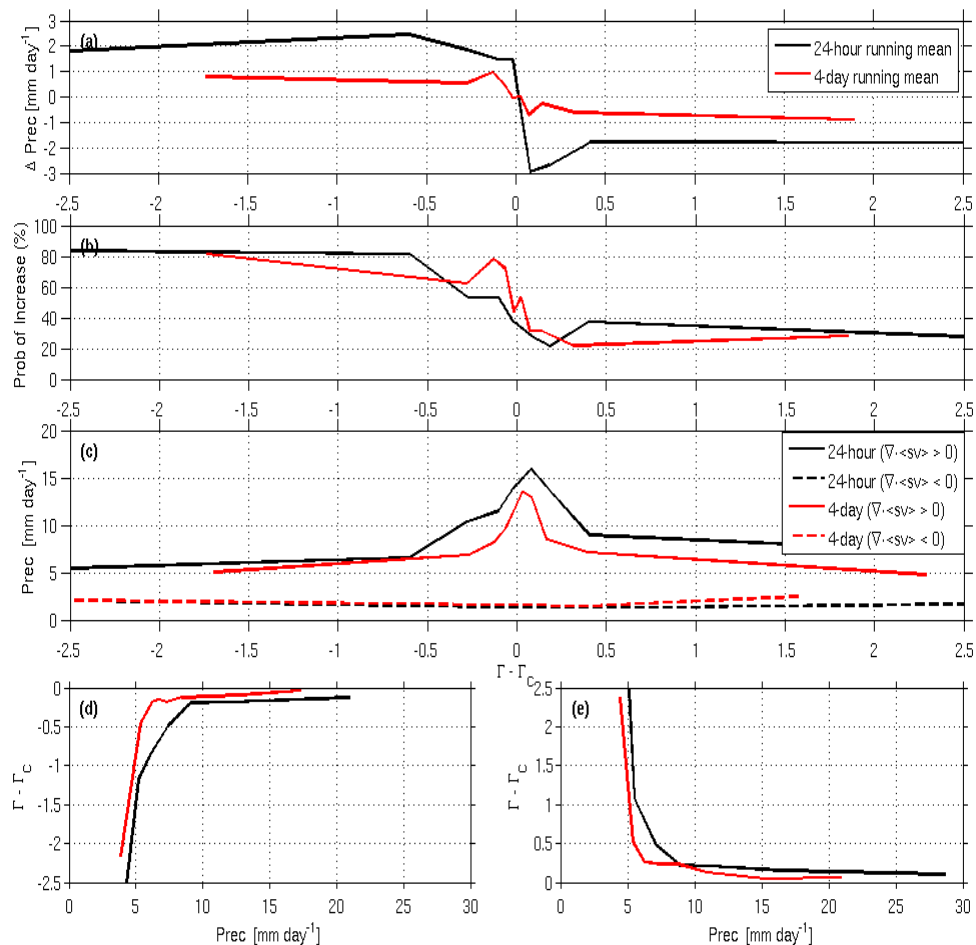


Figure 10: (a) Binned precipitation change as a function of GSM-criticality, averaged in 30-point-bins of GSM-criticality. (b) Binned probability of precipitation increase as a function of GSM-criticality, averaged in the same bins as (a). (c) Binned precipitation as a function of GSM-criticality, averaged in the same bins as above. (d) Binned GSM-criticality as a function of precipitation, averaged in 30-point-bins of precipitation in amplifying phase ($\Gamma - \Gamma_C < 0$). (e) As in (d), but for decaying phase ($\Gamma - \Gamma_C > 0$).

$\nabla \cdot \langle s\vec{v} \rangle$ is positive (these conditions correspond to cases when convection is active). The precipitation change at time i , ΔP_i , is computed by the center differencing, that is, $\Delta P_i = P_{i+1} - P_{i-1}$, and it is averaged within the bins which are constructed with respect to the GMS-criticality. Figure 10b illustrates binned probabilities of precipitation increase as a function of GMS-criticality for the events in which $\nabla \cdot \langle s\vec{v} \rangle$ is positive. These probabilities are computed by dividing the number of the events in each bin when the precipitation increases in the next time step by the number of the bin size. The bins are constructed in the same way as Fig. 10a. Figure 10c is a plot of binned precipitation versus GMS-criticality. The bins are constructed in the same way as above. The solid lines represent the cases in which $\nabla \cdot \langle s\vec{v} \rangle$ is positive (convective cases), and the dashed lines represent the cases in which $\nabla \cdot \langle s\vec{v} \rangle$ is negative (non-convective cases). Figures 10d and 10e represent binned GMS-criticality for convective cases ($\nabla \cdot \langle s\vec{v} \rangle > 0$) as a function of precipitation for the amplifying ($\Gamma - \Gamma_c < 0$) and decaying ($\Gamma - \Gamma_c > 0$) phases, respectively. For these panels, the bins are constructed with respect to the precipitation while the bins for the other panels are defined with respect to the GMS-criticality.

Figure 10a shows that when the GMS-criticality is negative (amplifying phase) the binned precipitation change is positive, which means the precipitation increases in the next time step in the self-amplifying phase. Conversely, when the GMS-criticality is positive (decaying phase) the corresponding precipitation change is negative, indicating the precipitation decreases in the next time step in the decaying phase. The black line represents the precipitation changes of 24-hour running mean filtered data, and the red

line corresponds to 4-day running mean filtered data. By taking a longer time mean, the magnitude of the precipitation changes becomes smaller, but the signals of the amplifying and decaying phases are robust for both time-scales.

Figure 10b illustrates that when the GMS-criticality is negative (amplifying phase) the precipitation increases with a high probability (>80%), and when the GMS-criticality is positive (decaying phase) the precipitation decreases with a high probability (60~75%).

If the theories of the amplifying and decaying phases were perfect and there were no measurement errors in the TOGA COARE data, this figure would look like a step function in which the precipitation increases at 100% when the GMS-criticality is negative and it decreases at 100% (or increases at 0%) when the GMS-criticality is positive. The 24-hour filtered data captures the general trends of the two phases, (p.1b) and (p.2b). Taking it into account that field campaign data generally contains a significant amount of noise and the numerator of the GMS, $\nabla \cdot \langle h\vec{v} \rangle$, is a difficult quantity to measure due to a large cancellation, this results seems to agree reasonably well with our hypotheses. By taking a longer time mean filter, the figure appears more like a step function, which is closer to our hypotheses, (p.1b) and (p.2b), implying that Eq. (10) makes more sense for longer time-scale events than for shorter time-scale events.

Now we want to look at Fig. 10c. When $\nabla \cdot \langle s\vec{v} \rangle$ is positive, the precipitation increases as the GMS-criticality gets closer to zero, and reaches its maximum value around zero GMS-criticality, which is predicted by Eq. (10). When $\nabla \cdot \langle s\vec{v} \rangle$ is negative, on the contrary, the precipitation takes small values over the whole range of the GMS-criticality. This is because the negative $\nabla \cdot \langle s\vec{v} \rangle$ corresponds to non-convective events in

which downward motion is dominant in the troposphere; in such a case the convection is, if any, very weak.

Figure 10d illustrates that when the GMS-criticality is negative (amplifying phase), the value of the GMS-criticality increases (or becomes less negative) as the precipitation increases, and eventually converges to zero. Conversely, when the GMS-criticality is positive (self-decaying phase), the value of the GMS-criticality increases (or becomes more positive) as the precipitation decreases (Fig. 10e).

The GMS-criticality represents the efficiency of MSE discharge by the convective system. Negative and large GMS-criticality indicates that the convective system efficiently imports MSE, and negative and close-to-zero GMS-criticality indicates that the MSE import is less efficient. Positive values of the GMS-criticality represent the efficiency of MSE export. Figs. 10d and 10e show that the convective system begins with high efficiency of MSE import, and as it develops, the efficiency of MSE import decrease. Eventually, the convective system starts to export MSE, and as it decays, the efficiency of MSE export increases.

Figures 10d and 10e, together with Fig. 10b indicate that the value of the GMS-criticality corresponds to the evolution of the convection. For instance, let's assume that a convective system begins in the amplifying phase, with some negative value of the GMS-criticality. According to Fig. 10b, the precipitation will increase in the next time step with a high probability, which means the value of the GMS-criticality will increase (or become less negative) in the next time step according to Fig. 10d. The GMS-criticality will keep increasing with a high probability as the convection develops, and eventually reach zero

at which point the precipitation reaches its maximum. After passing through the zero GMS-criticality, the convective system gets into the decaying phase, in which the precipitation will decrease with a high probability according to Fig. 10b, hence the value of the GMS-criticality will increase (or become more positive) in the next time step according to Fig. 10e. Therefore, the GMS-criticality starting from a negative value evolves into a positive value almost monotonically along with the convective evolution, implying that the value of the GMS-criticality, $\Gamma - \Gamma_C$, can be used as a diagnostic framework in which life-cycles of the convection can be investigated .

But why does the value of the GMS-criticality increase from negative to positive along with the evolution of the convection? And if it is true, then how does the value of the GMS-criticality come back to a negative value again? To address these issues, we need to consider a relationship between the GMS-criticality and convective life-cycles.

4.2 GMS-criticality and life-cycles of convection

Figure 11 illustrates evolutions of the vertical p-velocity (ω) profiles and the MSE profiles with respect to the GMS-criticality. Each variable is filtered by a 24-hour running mean. The MSE profiles are relatively constant compared with the ω profiles, which indicates that the advection of MSE is primarily regulated by variations of the ω profiles. In fact, most of the variations of the total MSE advection are due to the variations of the ω profiles, and the variations of the MSE profiles are less important. (Here, we assume the horizontal advection is a random process with respect to the convection as discussed in section 3. So the variances of the total MSE advection are the variances of the vertical advection which are primarily determined by the ω profiles plus some random noise.)

When the GMS-criticality is negative and large (≤ -1.0 , red curve in Fig. 11a), the ω profile has a bottom-heavy shape, which progressively deepens (black curve in Fig. 11a) and eventually evolves into a top-heavy profile having positive GMS-criticality (black curve in Fig. 11b). As the GMS-criticality increases more, this top-heavy profile weakens (pink curve in Fig. 11b), and at the same time downward motion starts to be developed in the lower troposphere (blue curve in Fig. 11b), which eventually causes negative $\nabla \cdot \langle s\vec{v} \rangle$ (Figs. 11c and 11d). When $\nabla \cdot \langle s\vec{v} \rangle$ is negative, downward motion is dominant over the whole troposphere. Eventually, new shallow convection in the lower troposphere starts to be developed (blue curve in Fig. 11d), which will evolve into bottom-heavy-shaped convection (red curve in Fig. 11a), making the life-cycle complete. One can see that the GMS-criticality monotonically increases as the convection evolves

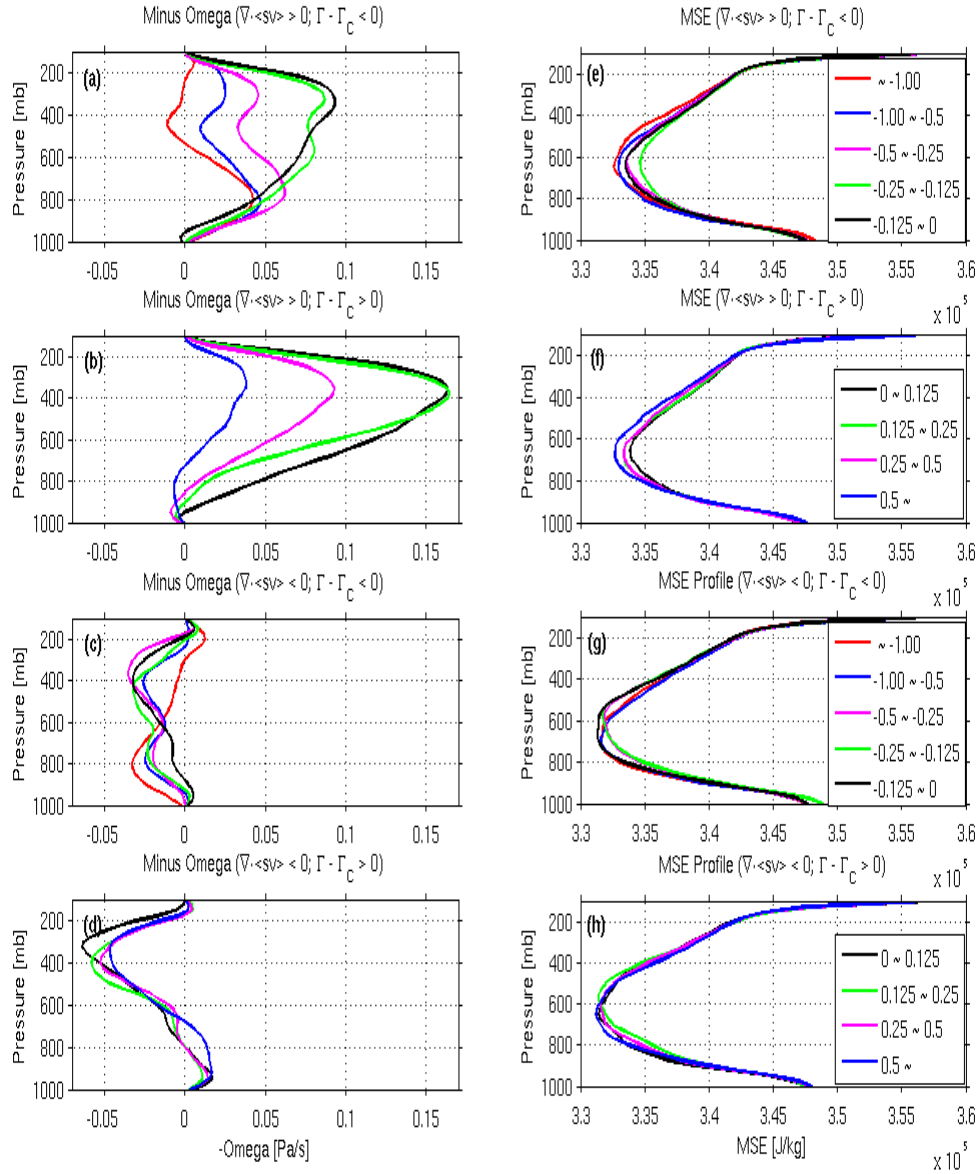


Figure 11: (a) Binned minus omega profiles for convective events ($\nabla \cdot \langle s\vec{v} \rangle > 0$), averaged in 30-point-bins of GMS -criticality in amplifying phase ($\Gamma - \Gamma_C < 0$). (b) As in (a), but for decaying phase ($\Gamma - \Gamma_C > 0$). (c) As in (a), but for non-convective events ($\nabla \cdot \langle s\vec{v} \rangle < 0$). (d) As in (b), but for non-convective events ($\nabla \cdot \langle s\vec{v} \rangle < 0$). (e) ~ (f) As in (a) ~ (d), for evolutions of MSE profile.

from a bottom-heavy shape into a top-heavy shape (Fig. 11a and 11b), and it reverses its processes when the downward motion is dominant (Fig. 11c and 11d).

Figure 12 is a schematic figure which depicts the relationship between the omega profiles and the GMS-criticality. To simplify the problem, let's assume that $F \equiv \langle Q_R \rangle + SF$ is equal to zero, which is not a bad assumption because F is usually small due to a cancellation between radiative cooling and surface fluxes. Furthermore, we assume that the horizontal MSE advection is zero in this schematic figure so that the total MSE advection is solely due to the vertical MSE advection. This assumption might be reasonable because as discussed in section 3 the horizontal MSE advection is approximately random so that the average value should be small. The schematic figure illustrates the average structure of the convection, thus we can ignore the horizontal advection in this figure. (This might be the most unclear statement in this thesis. In order to show that the horizontal advection doesn't affect the average convective structure, we should do the same analysis excluding the horizontal advection, and should show that the excluded horizontal advection doesn't affect the overall structures of the convection. This will be left for future study.) In those approximations, the amplifying and decaying phases are determined solely by the GMS, $\frac{\nabla \cdot \langle h\vec{v} \rangle}{\nabla \cdot \langle s\vec{v} \rangle}$ (especially vertical component of the GMS). Since both of the MSE and DSE profiles are relatively constant in the deep tropics, we assume these are fixed. The black lines represent omega profiles and the blue arrows illustrate associated large-scale circulations. The left-pointed and right-pointed arrows correspond to convergence and divergence of the flows, respectively.

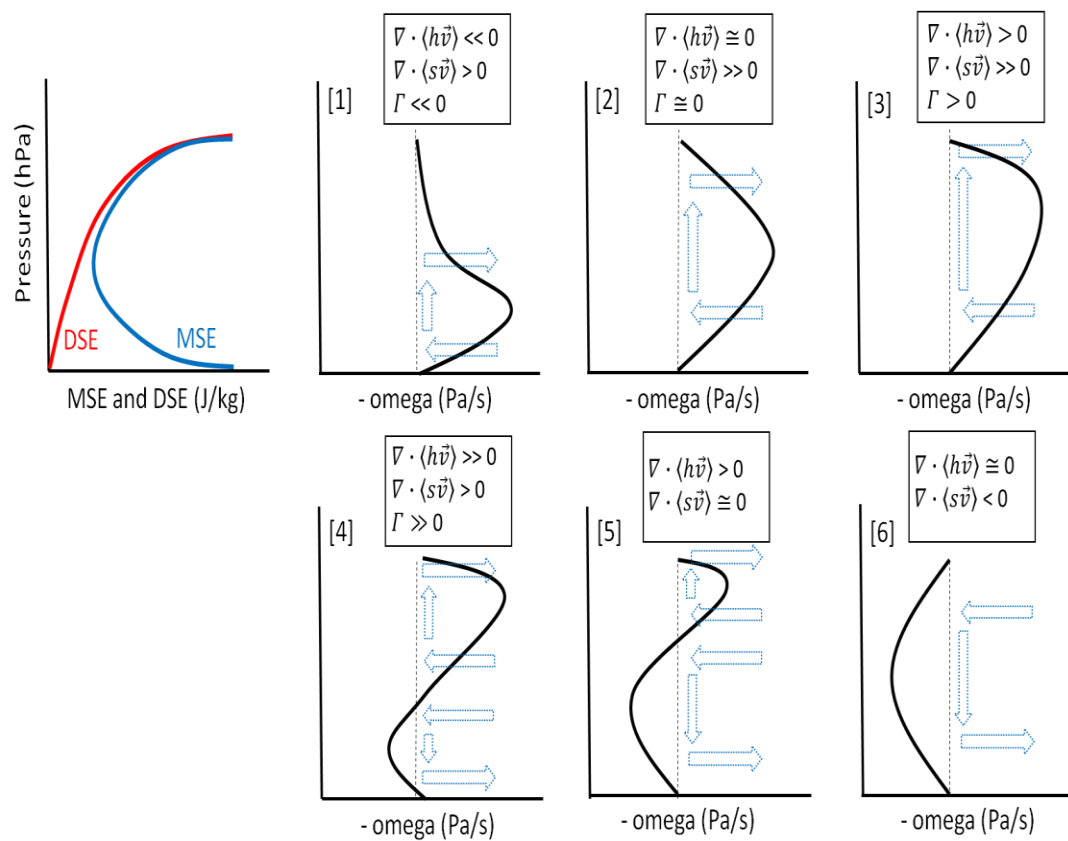


Figure 12: Idealized conceptualization of relation between GMS and convective evolution.

Moist convection starts with a bottom-heavy profile (Stage 1) in which convergence happens near the surface where MSE is rich and DSE is poor, and divergence happens in the middle troposphere where MSE is poor and DSE is moderate. As a result, large net MSE import ($\nabla \cdot \langle h\vec{v} \rangle \ll 0$) and moderate net DSE export ($\nabla \cdot \langle s\vec{v} \rangle > 0$) occur, causing negative and large GMS which leads to further enhancement of the convection. In Stage 2, exported MSE and imported MSE are approximately balanced, causing zero net MSE export, and hence zero GMS. The maximum precipitation is achieved in this stage under the assumption of zero F and zero horizontal advection. In the next stage (Stage 3), the vertical profile becomes a top-heavy profile in which air with moderate MSE and poor DSE is imported and air with rich MSE and rich DSE is exported, causing moderate net MSE export ($\nabla \cdot \langle h\vec{v} \rangle > 0$) and large net DSE export ($\nabla \cdot \langle s\vec{v} \rangle \gg 0$), hence the corresponding GMS is positive and small which leads to decay of the convection in the next time step. Since $F \equiv \langle Q_R \rangle + SF$ is not zero but small and positive in general, the maximum precipitation is usually expected to be achieved in this stage.

After the peak of the convection (Stage 4), lower tropospheric downward motion with surface divergence is observed, which exports MSE efficiently ($\nabla \cdot \langle h\vec{v} \rangle \gg 0$), causing positive and large GMS. In this stage, MSE is discharged most efficiently, which dries out the system, leading to further decay of the convection. The maximum value of the GMS is generally achieved in this stage since the vertical structure with middle tropospheric convergence and upper and lower tropospheric divergence is most efficient for MSE export. In the next stage where the downward motion is dominant in the lower

troposphere (Stage 5), the GMS cannot be defined because the denominator of the GMS, net DSE export, is approximately zero. In Stage 6, the downward motion is dominant over the whole troposphere, and the exported MSE and the imported MSE are balanced, causing zero GMS again. The minimum precipitation is expected to happen in this stage.

4.3 Effects of radiative heating and surface flux

In the above arguments, we verified that the convection is actually amplified and attenuated in the amplifying and decaying phases which we hypothesized. However, our original hypothesis is that the amplification or decay is primarily regulated by the variation of vertical velocity profiles. Since the GMS-criticality, $\Gamma - \Gamma_c$, includes radiative heating and surface flux in its definition, we cannot conclude that the amplification or decay is due to the vertical velocity profiles. It might be possible that the radiative heating and surface flux play a dominant role in the amplification mechanism. Therefore, in order to further our argument, we need to look at the effect of the radiative heating and surface flux on the convective system

Figure 13 represents binned precipitations and binned omega structures with respect to the GMS (top panel) and the GMS-criticality (bottom panel). Each quantity is daily averaged. By comparing those two panels, we can infer the coupling effects of the radiative heating and surface flux to the convective property.

The main difference between those is the value at which the strongest convection happens. The top panel shows that the strongest convection happens when the GMS is about 0.4 while the bottom panel shows that the strongest convection happens when the

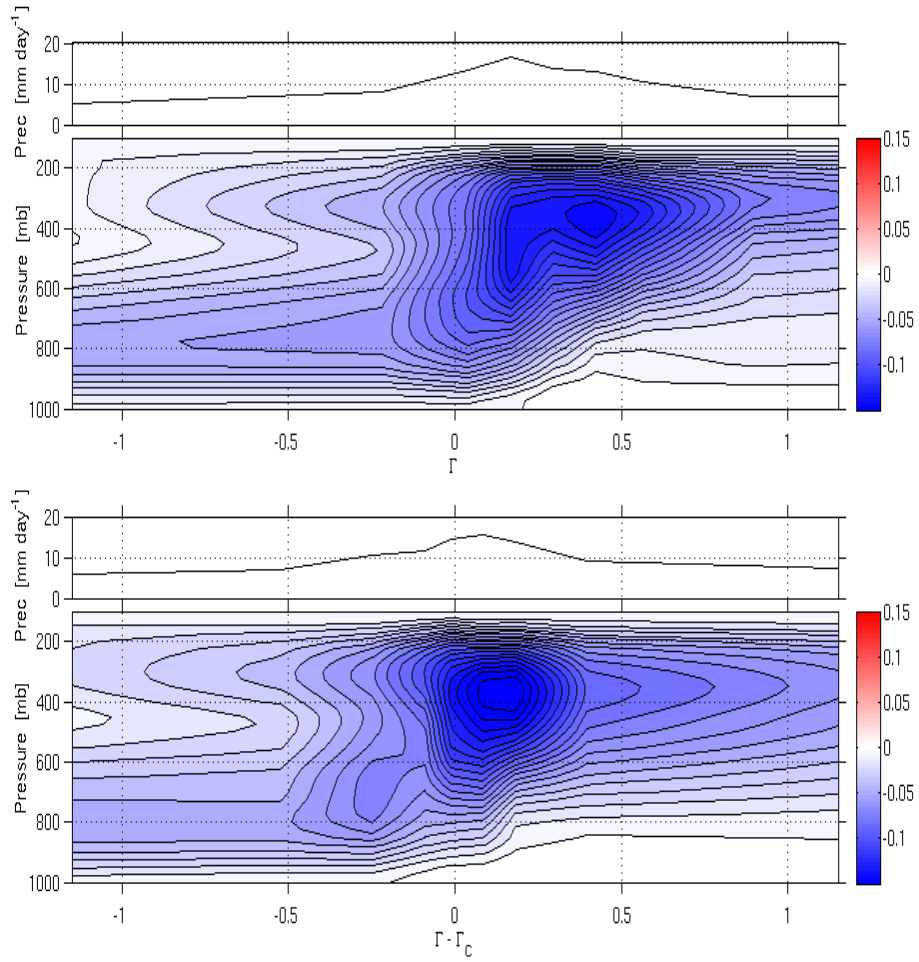


Figure 13: (Top two panels) Binned precipitation and binned omega profile, averaged in 30-point-bins with respect to GMS. (Bottom two panels) As in the top two panels, but averaged in bins of GMS-criticality.

GMS-criticality is about 0.2. Thus the main effect of the radiative heating plus surface flux on the convective structure is the shift of the convective peak toward the left of the figure by 0.2. What does this shift imply?

This question can be addressed by looking at Fig. 14, which shows in the top row the minus total MSE advection (or column MSE flux divergence), $\nabla \cdot \langle h\vec{v} \rangle$, and radiative heating plus surface flux, $F \equiv \langle Q_R \rangle + SF$, as a function of minus DSE advection (or column DSE flux divergence), $\nabla \cdot \langle s\vec{v} \rangle$, and in the bottom row the PDFs of the GMS, $\frac{\nabla \cdot \langle h\vec{v} \rangle}{\nabla \cdot \langle s\vec{v} \rangle}$ and critical-GMS, $\frac{F}{\nabla \cdot \langle s\vec{v} \rangle}$ for convective cases ($\nabla \cdot \langle s\vec{v} \rangle > 0$). One can notice that $F \equiv \langle Q_R \rangle + SF$ is more linearly correlated to $\nabla \cdot \langle s\vec{v} \rangle$ than $\nabla \cdot \langle h\vec{v} \rangle$ is. (The correlation coefficient of the former is 0.63 while that of the latter is 0.48.) As a result, variances of the critical-GMS are smaller than those of the GMS, concentrating around the mean value ~ 0.2 . This mean value of the critical-GMS corresponds to the slope of F versus $\nabla \cdot \langle s\vec{v} \rangle$ plot, and also to the value of the shift of the convective peak in Fig. 13.

The definition of the GMS-criticality is the GMS minus critical-GMS, $\Gamma - \Gamma_C \equiv \frac{\nabla \cdot \langle h\vec{v} \rangle}{\nabla \cdot \langle s\vec{v} \rangle} - \frac{F}{\nabla \cdot \langle s\vec{v} \rangle}$, and its physical meaning is the efficiency of moisture (or MSE) discharge by the convective system. Thus the GMS and critical-GMS, respectively, represent the efficiency of the moisture discharge (or MSE discharge) via advection and via radiative heating plus surface flux. Since the radiative heating plus surface flux is more linear with respect to the intensity of the convection ($\nabla \cdot \langle s\vec{v} \rangle$ is approximately equal to the precipitation rate) than the MSE advection is, as a result, the GMS criticality becomes $\Gamma - \Gamma_C \approx \frac{\nabla \cdot \langle h\vec{v} \rangle}{\nabla \cdot \langle s\vec{v} \rangle} - \text{constant}$. This means the moisture (MSE) discharge

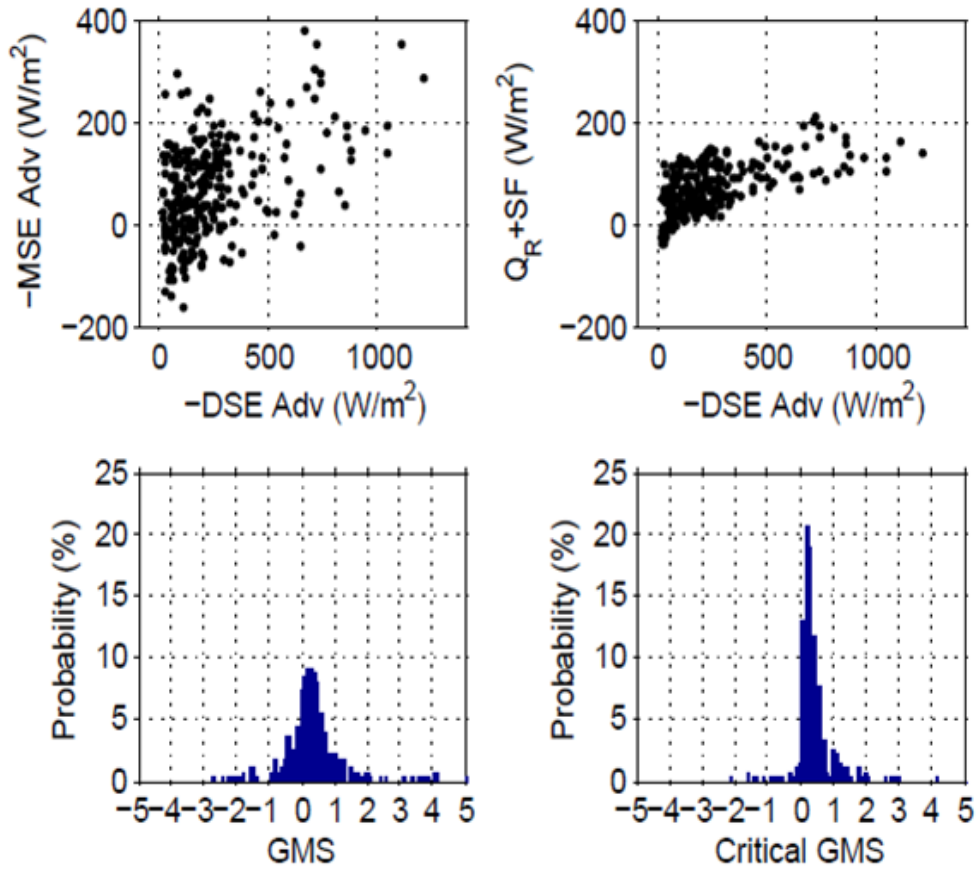


Figure 14: (Up left) Negative total MSE advection $\nabla \cdot \langle h\vec{v} \rangle$ as a function of negative total DSE advection $\nabla \cdot \langle s\vec{v} \rangle$. (Up right) Radiative heating plus surface flux as a function of negative total DSE advection $\nabla \cdot \langle s\vec{v} \rangle$. (Bottom left) PDF of GMS. (Bottom right) PDF of critical-GMS.

efficiency via radiative heating plus surface flux is relatively constant through the life-cycle of the convection while the efficiency via advection varies. This fact indicates that the variation of the moisture (MSE) discharge efficiency is primarily due to the variances of the vertical advection (since the horizontal advection is relatively random) which is regulated by the shape of the omega profile.

Based on the argument above, we can infer one important implication regarding the tropical convection: As the convection develops, the efficiency of the moisture discharge changes and that variation is mainly regulated by the variation of the omega profile shape.

5. Modification of theory

As discussed above, the GMS, together with the critical GMS, can be used as an indicator of the life-cycle of the moist convection. However, the GMS defined by Eq. (1) is only applicable to the cases in which the convection had developed enough. In the beginning stage of the convection, upward motion is confined in the lower troposphere exhibiting a bottom-heavy profile (see Stage 1 in Fig. 12). But real shallow convection generally, unlike Fig. 12, accompanies upper tropospheric subsidence with strong convergence in the upper troposphere which imports DSE-rich air, causing negative $\nabla \cdot \langle s\vec{v} \rangle$. If the convection develops enough (like Stage 1 in Fig. 12), conversely, the DSE is exported from the atmospheric column, causing positive $\nabla \cdot \langle s\vec{v} \rangle$. Therefore, due to the singularity, the GMS cannot be continuously defined over the episode of the convective life-cycle which evolves from a shallow and weak to a mature stage. This limitation motivates us to define a new quantity, called modified GMS (MGMS), by adding a small modification on the definition of the GMS.

We define the modified gross moist stability (MGMS) by

$$\Gamma_M \equiv \frac{\nabla \cdot \langle h\vec{v} \rangle}{\nabla \cdot \langle s\vec{v} \rangle - \langle Q_R \rangle}. \quad (12)$$

The main advantage for this definition is that the denominator of the MGMS is guaranteed to be positive for most of the cases, which is the motivation for deriving this quantity. According to Eq. (6), the denominator of Γ_M is approximately balanced by $LP + SH$ which is always positive. Since the DSE tendency term in Eq. (4) which was

assumed to be negligible is not perfectly zero, the denominator sometimes becomes negative, but that accounts for only 10% of the total measurements, which are excluded from our analysis. Therefore, the MGMS is applicable even to shallow convection which accompanies upper tropospheric downward motion, making it possible to explore a relationship between the MGMS and evolutions of complex vertical structures of the moist convection. Since the denominator of the MGMS still represents intensity of the convection (which is approximately equal to the precipitation), this version of GMS works in a similar manner to the other version of GMS. (In fact, Andersen and Kuang (2011) used a similar definition to Eq. (12), and they called it the GMS).

Another advantage regarding the MGMS is that it is more mathematically tractable than the conventional GMS, making the relationship between the moisture discharge and development of the convection clearer. More specifically, we can represent the intensity of the convection as a function of the MGMS. This will be described in section 6 where the behavior of the MGMS is examined.

Similarly to the conventional GMS, we define the critical MGMS as

$$\Gamma_{CM} \equiv \frac{\langle Q_R \rangle + SF}{\nabla \cdot \langle S\vec{v} \rangle - \langle Q_R \rangle}. \quad (13)$$

The amplifying and decaying phases are, respectively, expressed as

$$\Gamma_M - \Gamma_{CM} < 0 \quad (\text{p.1d})$$

$$\Gamma_M - \Gamma_{CM} > 0. \quad (\text{p.2d})$$

Now we name the quantity, $\Gamma_M - \Gamma_{CM}$, MGMS-criticality. We can interpret the physical meaning of the MGM-criticality in the same way as the standard GMS-criticality. That is, the value of MGMS-criticality represents the efficiency of moisture discharge (or

recharge) per unit intensity of the convection. Negative and large MGMS-criticality indicates that the convection possesses an efficient structure for a moisture recharge while positive and large MGMS-criticality corresponds to an efficient structure for a moisture discharge.

6. Results and discussion II: MGMS-criticality and convection

In this section, we examine the relations between the MGMS-criticality and convective properties by using the same analysis methods as in section 4. One of the main points in this section is to point out that the MGMS-criticality works in the same way as the GMS-criticality described in section 4. We also want to further our arguments regarding convective properties using the MGMS-criticality.

6.1 MGMS-criticality and amplifying or decaying phases

Since we are only interested in the cases in which convection is happening, we want to exclude non-convective cases in which downward motion is dominant over the troposphere. For the standard GMS, we did that task by using the threshold of positive $\nabla \cdot \langle s\vec{v} \rangle$. But this threshold excludes too many measurements, some of which correspond to weakly convective cases. Thus, for removing non-convective cases, a new quantity which indicates dominance of descending motion is introduced.

First of all, we separate the upward and downward components of the vertical velocity by

$$\omega^- \equiv \max(-\omega, 0) \quad (14)$$

$$\omega^+ \equiv \max(\omega, 0) \quad (15)$$

and define the new indicator by

$$I = \frac{\int_{P_S}^{P_M} \omega^+ dp}{\int_{P_S}^{P_M} (\omega^+ + \omega^-) dp} \quad (16)$$

where P_M and P_S are, respectively, the middle tropospheric pressure (500 hPa) and the surface pressure (1000 hPa). This indicator represents how dominant downward motion is in the lower half of the middle troposphere. If this quantity is close to unity the motion which happens below the middle troposphere is predominantly descending. Conversely, a small value of I indicates that upward motion is significant in the lower half of the troposphere. We define a non-convective event as an event whose I is greater than 0.5. This threshold method is arbitrary to some extent, and there are other possible ways to separate the convective and non-convective cases. We tried a couple other methods, and found this method efficient enough.

Now we examine our modified theory in the TOGA COARE data set. Figure 15 is the same kind of plot as Fig. 10, but the GMS-criticality in Fig. 10 is changed into the MGMS-criticality. We exclude the events whose $\nabla \cdot \langle s\vec{v} \rangle - \langle Q_R \rangle$ is less than 0.5 W m^{-2} in order to avoid division by zero. For all the panels except for Fig. 15c, plotted are only convective cases in which I is less than 0.5. All bins are constructed in the same way as Fig. 10.

Figures 15a and 15b show that when the MGMS-criticality is negative (amplifying phase), the bin-averaged precipitation changes are positive, and the precipitation will increase in the next time step with a high probability. Conversely, when the MGMS-criticality is positive (decaying phase) the bin-averaged precipitation changes are negative, and the precipitation will decrease with a high probability. By taking a

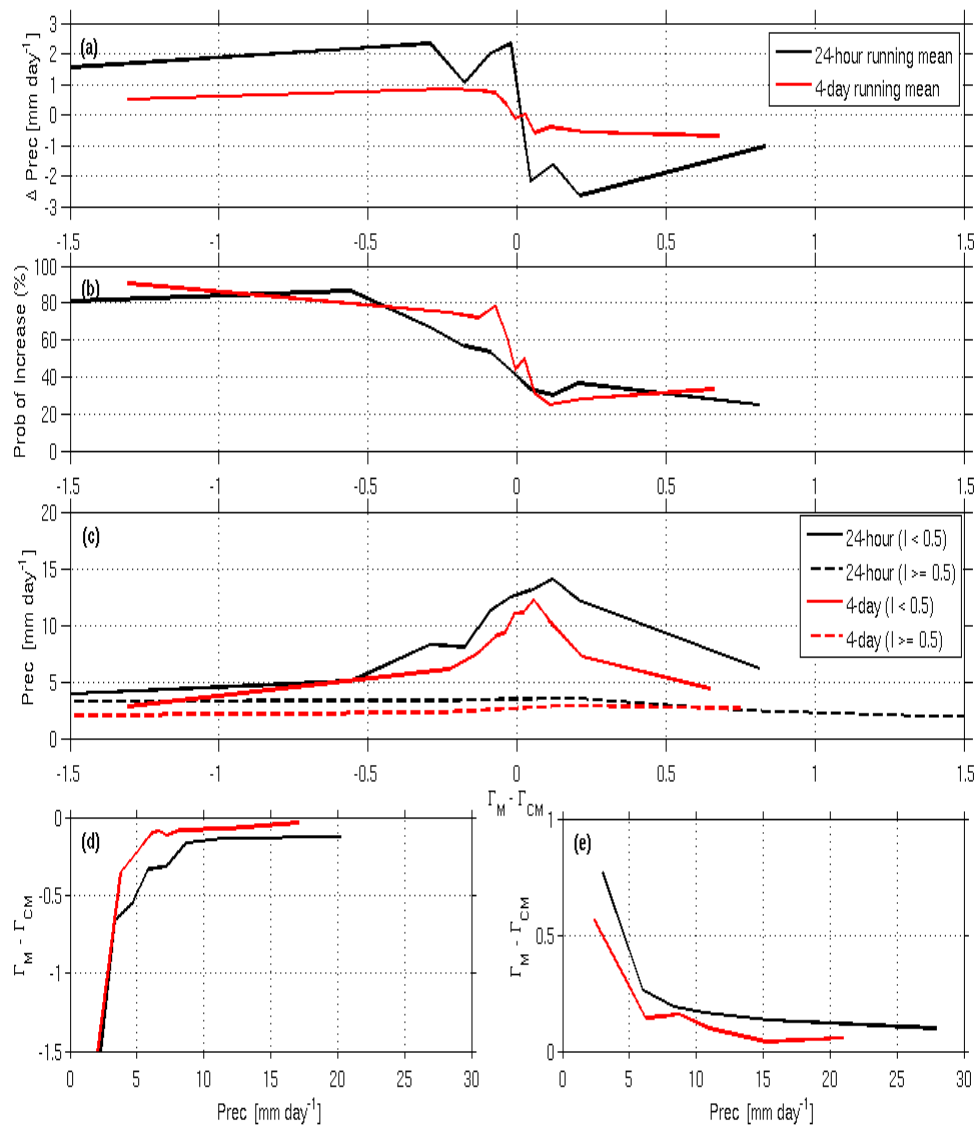


Figure 15: As in Fig. 10, but for MGMS-criticality.

longer time mean filter, Fig 15b appears more like a step function. That is because the assumption of negligible temperature anomalies becomes more accurate in longer time-scale variability.

Figure 15c is a plot of binned precipitations versus binned MGMS-criticality. The solid lines represent the cases where upward motion is dominant ($I < 0.5$), and the dashed lines corresponds to non-convective cases ($I \geq 0.5$). For the convective cases, the precipitation increases as the MGMS-criticality gets closer to zero. For non-convective cases, in contrast, precipitation takes small values over the whole range of the MGMS-criticality. This result indicates that we successfully separated the convective and non-convective cases by using the indicator defined by Eq. (16).

Figure 15d shows that, in the amplifying phase, the MGMS-criticality becomes greater (or less negative) as the precipitation increases. Conversely, Fig 15e illustrates that, in the decaying phase, the MGMS-criticality becomes greater (or more positive) as the precipitation decreases. Both of the figures represent only convective events ($I < 0.5$).

As discussed in section 4, Fig. 15d and 15e, together with Fig. 15b, imply that the MGMS-criticality can indicate evolution of moist convection. The MGMS-criticality, starting with a negative value, monotonically increases to a positive value as the moist convection develops from shallow to deep convection, and the reverse process happens when downward motion is dominant. In the amplifying phase, the moist convection starts with a structure which recharges moisture efficiently (negative and large MGMS-criticality), leading to further enhancement of the convection in the next step. The convection steadily evolves into a structure which recharges moisture less efficiently

(negative and small MGMS-criticality), and eventually gets into the decaying phase after the precipitation peak. In the decaying phase, the convection and its associated large-scale circulations export moisture from the atmospheric column, which dries out the system and causes further decay of the convection.

6.2 Vertical structures of omega and wind divergence

In Fig. 16, plotted are binned precipitation, binned omega and wind divergence profiles with respect to the binned MGMS-criticality. In this figure, all the non-convective cases ($I \geq 0.5$) are excluded, and each quantity is filtered by a 24-hour running mean. Since the MGMS-criticality indicates the evolution of the convective life-cycles, those contour plots can be thought of as time-height structures. We should note, however, that the interval of the MGMS-criticality is not proportional to the actual time interval. The MGMS-criticality simply illustrates that the moist convection evolves from a negative to a positive value of the MGMS-criticality. As discussed in the section 4.3, the efficiency of moisture discharge is primarily controlled by the shape of omega profiles. Figure 16, therefore, can be used in order to infer the relationship between the omega profile and moisture discharge efficiency.

In the beginning stage of the amplifying phase, the omega structure exhibits a bottom-heavy profile whose peak is located at around 800 hPa. Together with the bottom-heavy shallow convection, there exists upper tropospheric downward motion. The corresponding wind divergence field possesses strong surface and upper tropospheric convergence and strong middle tropospheric divergence. The surface convergence is

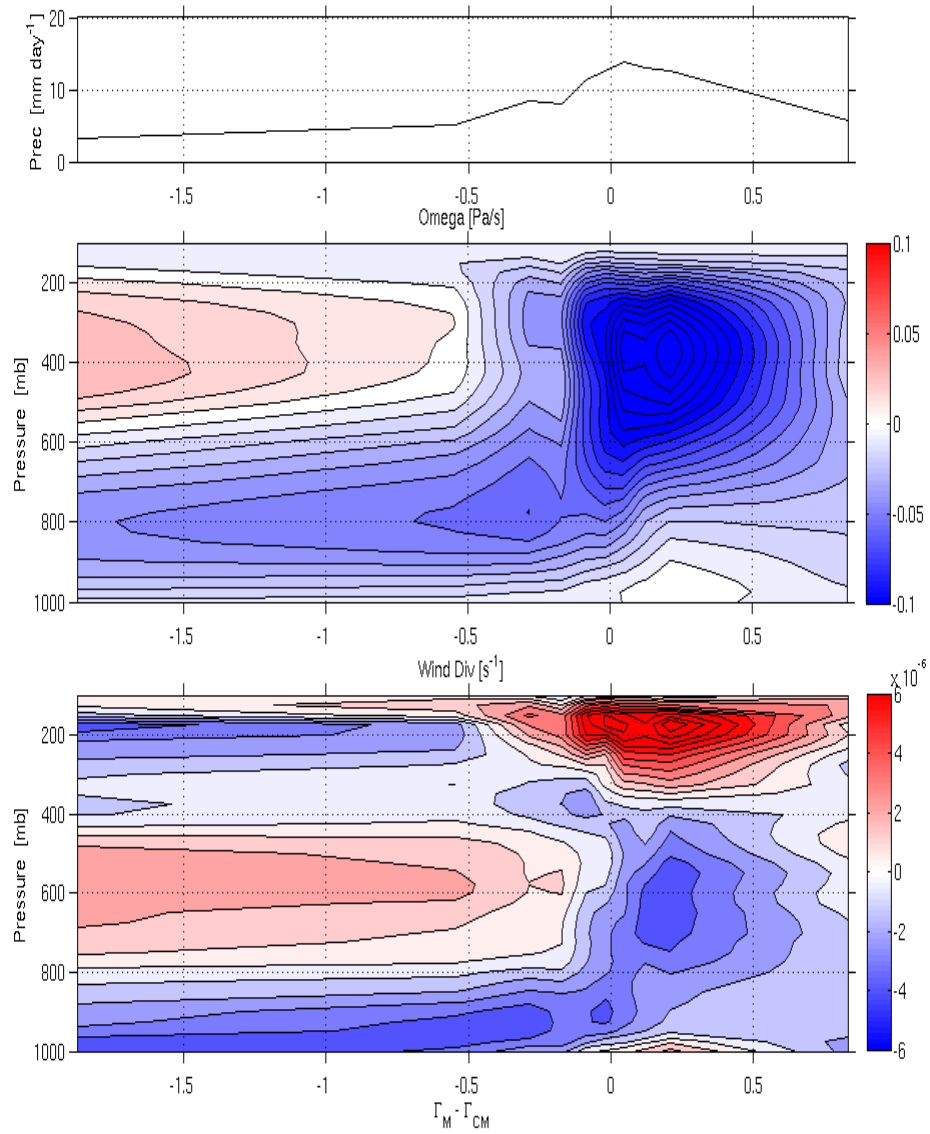


Figure 16: (Top) Binned precipitation as a function of MGMS-criticality, averaged in 30-point-bins of MGMS-criticality. (Middle) Binned omega profiles as a function of MGMS-criticality, averaged in the same bins as the top panel. (Bottom) As in the middle panel, but for wind divergence profiles

responsible for the moisture import, which moistens the system and augments the moist convection. The upper tropospheric convergence imports DSE-rich air (thus MSE-rich air), and the middle tropospheric divergence exports MSE-poor air, enhancing the column MSE import via vertical advection. As the MGMS-criticality becomes less negative (which means the moist convection develops), the lower tropospheric shallow convection is strengthened while the upper tropospheric subsidence is weakened.

It's worth pointing out that the bottom-heaviness which is efficient for moisture import is persistent until the upper tropospheric descending motion disappears ($\Gamma_M - \Gamma_{CM}$ is around -0.5). This result would imply that the upper tropospheric downward motion plays an important role in the buildup of MSE by preventing the bottom-heavy profile from becoming a deep top-heavy profile, enhancing the surface convergence which imports moisture efficiently. This is consistent with previous studies such as Stephens et al. (2004) and Kikuchi and Takayabu (2004).

When the MGMS-criticality is negative and small (around -0.25), bimodal patterns of omega whose dual peaks are located at around 300 hPa and 700 hPa can be seen. This bimodal signal is also robust in the wind divergence field, exhibiting a quadruple (- + - +) structure. This structure has been pointed out by Mapes et al. (2006), who have claimed that this bimodal signal may have some physical meaning.

When the MGMS-criticality is positive (decaying phase), the omega profile possesses a top-heavy shape with strong upper-tropospheric divergence and moderate surface divergence, which export MSE from the atmospheric column, leading to further decay of the moist convection.

Figure 17 illustrates time-height structures of omega and wind divergence fields in the TOGA COARE field experiment. Each quantity is filtered with a 4-day running mean. These observations support the idea that the MGMS-criticality binning method captures the life-cycle of moist convection. Each convective episode starts with a bottom-heavy profile and strong surface convergence, which progressively develops into a top-heavy profile. In the buildup stages, strong upper tropospheric subsidence and its associated strong upper tropospheric convergence can be observed. One can also see the bimodal structures in the omega field (emphasized by black boxes) and in the wind divergence field (emphasized by dashed black boxes).

6.3 Vertical structures of anomalous DSE and moisture

Figure 18 shows binned radiative cooling, $-\langle Q_R \rangle$, and surface flux, $SF \equiv LE + SH$, with binned vertical structures of anomalous DSE and moisture with respect to the MGMS-criticality for convective events. Each quantity is daily averaged. The DSE anomaly is equivalent to the temperature anomaly. (The mean profile of the DSE is monotonically increasing with height while that of the moisture is monotonically decreasing with height.)

First, it should be noted that the magnitude of the anomalous moisture is about 4 times larger than that of anomalous DSE, causing the variances of vertically integrated moisture to be much larger than those of vertically integrated DSE as we assumed in the previous sections. The surface flux increases as the convection develops, which is partially due to strengthened surface winds and gustiness caused by downdrafts in deep convection. The timing of the peak slightly lags the convective peak. The radiative

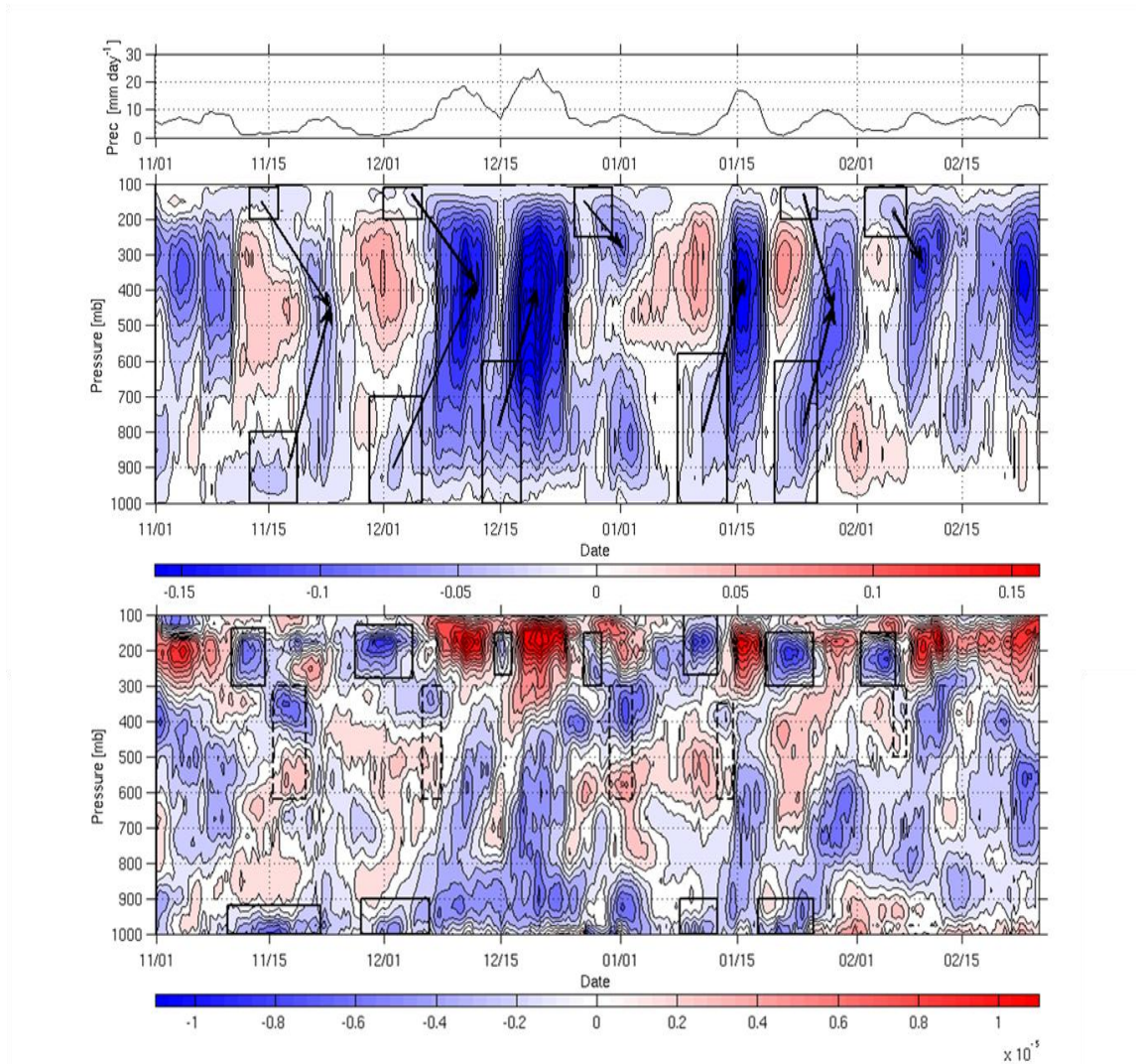


Figure 17: (Top) Time-series of 4-day running averaged precipitation during TOGA COARE. (Middle) Time-height structure of 4-day running averaged omega profiles. (Bottom) Corresponding divergence structure. The black boxes and arrows emphasize lower tropospheric tilting omega profiles and upper tropospheric bimodal omega structures.

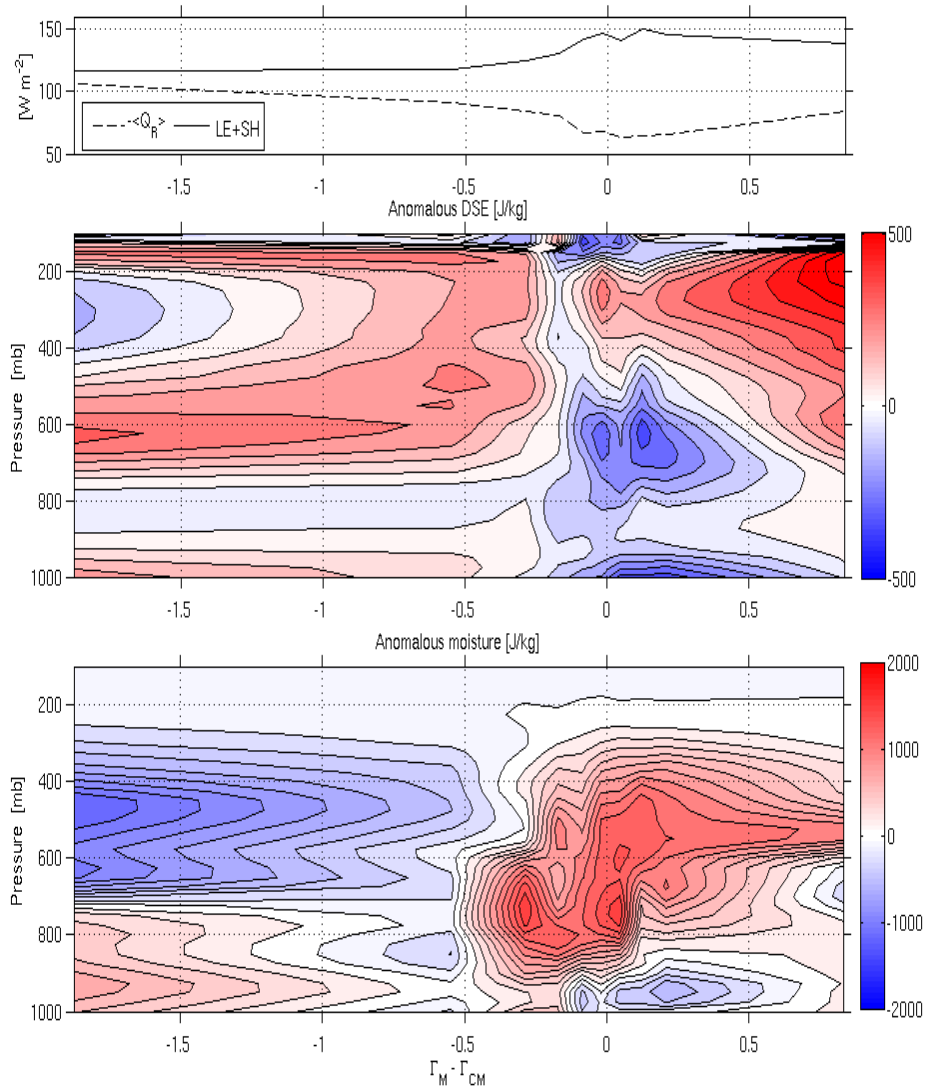


Figure 18: (Top) Binned radiative cooling and surface flux as a function of MGMS-criticality, averaged in 30-point-bins of MGMS-criticality. (Middle) Binned DSE anomaly profiles as a function of MGMS-criticality, averaged in the same bins as the top panel. (Bottom) As in the middle panel, but for moisture anomaly profiles.

cooling decreases as the convection develops because of increase in cloudiness and cloud top height which decrease longwave radiation escaping into the space. The gap between the lines of the radiative cooling and the surface flux (or the area surrounded by those lines) represents the amount of $F \equiv \langle Q_R \rangle + SF$, as discussed in section 4.3 which has a positive linear proportionality to the intensity of the convection .

When the MGMS-criticality is negative and large, positive anomalies of the DSE can be observed in the boundary layer, which destabilize the lower troposphere, enhancing the shallow convection. This anomalously warm boundary layer might be ascribed to anomalously high SST in the suppression phase of the convection (Stephens et al. 2004).

Negative MGMS-criticality is characterized by a warm layer around 600 hPa, which makes the atmospheric column anomalously stable so that the shallow convection cannot penetrate this layer, maintaining the bottom-heaviness with strong surface convergence which recharges moisture. This anomalously warm middle troposphere might correspond to the 0 °C inversion and trade inversion which are pointed out by Kukuchi and Takayabu (2004) and Johnson et al. (1999).

When the MGMS-criticality becomes around -0.5, the whole upper troposphere is warmed up, making the atmospheric column “thermodynamically” more stable. In this system, however, a buildup of moisture happens and the convection is being developed, thus this system could be characterized as in an unstable condition from this perspective. In this system, the thermodynamically more stable atmosphere enhances the moisture

recharge by maintaining the bottom-heaviness of the convection, making a favorable condition for the moist convection and destabilizing the convective system.

The moisture figure (third panel in Fig. 18) shows that in the beginning stage of the amplifying phase, positive anomalies are confined in the lower troposphere while the upper-troposphere is very dry, causing significant moisture stratification in this stage. As the convection develops, the negative anomalies of moisture are weakened, indicating steady transport of moisture into the upper-troposphere. After passing the MGMS-criticality -0.5, the whole troposphere is moistened significantly. After the peak of the precipitation, negative anomalies can be observed near the surface, which might be a result of the surface divergence and downdrafts of dry air. The overall structures in Fig. 18 are consistent with the results of the statistical composite analysis of the TOGA COARE data by Mapes et al. (2006).

6.4 MGMS-criticality and intensity of convection

As mentioned earlier, one of the advantages regarding the modification of the conventional GMS is mathematical tractability; we can express intensity of precipitation as a function of the MGMS and critical-MGMS. By using the MGMS-criticality, $\Gamma_M - \Gamma_{CM}$, Eqs. (6) and (10) can be combined into

$$\frac{\partial \ln P}{\partial t} = -\alpha(\Gamma_M - \Gamma_{CM})P \left(1 + \frac{SH}{LP}\right). \quad (17)$$

Since $\frac{SH}{LP}$ is generally negligible, we obtain

$$\frac{\partial P}{\partial t} = -\alpha(\Gamma_M - \Gamma_{CM})P^2. \quad (18)$$

Solving this differential equation yields

$$P = \frac{P_0}{1 + \alpha P_0 \int_{t_0}^t (\Gamma_M - \Gamma_{CM}) ds} \quad (19)$$

where t_0 is some reference time and P_0 is a reference precipitation at time t_0 . Equation (19) indicates that the longer a system stays in the amplifying phase ($\Gamma_M - \Gamma_{CM} < 0$), the more intense the following precipitation becomes. Recalling Figs. 16 and 18, an anomalously warm middle troposphere prevents shallow convection from developing into a top-heavy shape, which enhances the MSE import, making $\Gamma_M - \Gamma_{CM}$ more negative. Equation (19), together with Fig. 16 and 18, suggest a great importance of a shallow convective regime in which a buildup of MSE happens via shallow vertical motions and associated shallow circulations, which was pointed out by previous studies (e.g., Johnson et al. 1999; Kikuchi and Takayabu 2000; Benedict and Randall 2007; Stephens et al 2004.)

Furthermore, utilizing the linearity of $F \equiv \langle Q_R \rangle + SF$ with respect to the intensity of the convection as discussed in section 4.3, we can infer $\Gamma_{CM} \approx \gamma$, where γ is a constant slope which is computed from the plot of F versus precipitation. Therefore, Eq. (19) can be written as

$$P = \frac{P_0}{1 + \alpha P_0 \left(\int_{t_0}^t \Gamma_M ds - \gamma \Delta t \right)}. \quad (20)$$

In this equation, the only variable is Γ_M , which is mainly determined by the shape of the omega profile. By examining Eq. (20), therefore, we might be able to infer the relation between omega profile shape and precipitation.

7. Conclusion

The main hypothesis we presented was the following: Convection is amplified via negative (or effectively negative) GMS which corresponds to a bottom-heavy vertical velocity profile which efficiently imports MSE into the convective system. Convection is, in contrast, attenuated via positive (or effectively positive) GMS which is associated with a top-heavy vertical velocity profile which exports MSE from the atmospheric column, making the convective system drier, and thus making the system less favorable for convection. In order to show that this main hypothesis is true, we had to verify the following two small hypotheses.

1. Convection is really amplified (or attenuated) via effectively negative (positive) GMS.
2. If hypothesis 1 is true, then the amplification (or attenuation) is primarily regulated by the shape of the vertical velocity profile.

The verification of hypothesis 1 was relatively straightforward. Figures 10a and 10b show that the precipitation is enhanced when the GMS is less than the critical value ($\Gamma - \Gamma_c < 0$), and is weakened when the GMS is greater than the critical value ($\Gamma - \Gamma_c > 0$). This suggests that the theory of amplification and decay works. Then now, what we want to show is that the amplification or decay is primarily regulated by the vertical velocity profiles. Since the definition of the GMS-criticality $\Gamma - \Gamma_c$ contains radiative heating and surface flux, it might be possible that the radiative heating or surface flux is

the primary regulator of the convective amplification. In order to verify hypothesis 2, we took a chain of non-trivial logics.

First, we examined the effect of radiative heating and surface flux on the convective structure by comparing two figures in Fig. 13. Although there are small differences in detail, those two figures show a qualitatively similar structure. The main difference between them is the value of the GMS (or GMS-criticality) at which the convective peak happens. In the GMS figure the convective peak happens when the GMS is about 0.4 while in the GMS-criticality figure the maximum convection happens when the value of the GMS-criticality is about 0.2. Thus we inferred that the main effect of the radiative heating plus surface flux on the convective system is to shift the timing of the convective peak. What is the physical implication of that difference?

To answer that question, we examined Fig. 14, which shows $\nabla \cdot \langle h\vec{v} \rangle$ and $F \equiv \langle Q_R \rangle + SF$ as a function of $\nabla \cdot \langle s\vec{v} \rangle$. From this figure, we can observe that the $F \equiv \langle Q_R \rangle + SF$ is more linearly correlated to $\nabla \cdot \langle s\vec{v} \rangle$ than $\nabla \cdot \langle h\vec{v} \rangle$ is. This linearity causes the critical GMS to be relatively constant. (You can compare the PDFs of the GMS and critical-GMS). The critical-GMS represents the efficiency of moisture recharge due to the radiative heating and surface flux. Since this is more constant than the GMS, variances of the total efficiency of moisture discharge, GMS-criticality, are more due to the advection rather than the radiative heating and surface flux. Since we argued for shorter time-scale variability the horizontal advection is relatively random, and not correlated to the convective system, we might be able to conclude that the variances of

the moisture discharge efficiency are primarily regulated by the vertical motions. Thus the amplification mechanism is mainly controlled by the vertical velocity profiles.

In section 5, we introduced a new quantity called MGMS and MGMS-criticality. By using those quantities, we can examine the relationship between atmospheric structures, vertical velocity profiles, and convective amplification. That relationship is summarized in the schematic figure shown in Fig. 19. In the very beginning stage, the lower troposphere is destabilized by the surface layer warming, initializing the shallow convection. This shallow convection with a bottom-heavy shape efficiently imports moisture via low level convergence (negative GMS), leading to further enhancement of the convection. However, due to the temperature inversion in the middle troposphere, the bottom-heaviness cannot penetrate this inversion, causing further enhancement of the bottom-heaviness. That enhanced bottom-heavy convection imports more moisture than the previous stage, making the lower troposphere very moist and favorable for further convection. Eventually, the inversion disappears, which enables the convection to become top-heavy, and that deepened convection transports moisture into the upper troposphere. This conceptual amplification can be observed in the MJO dynamics (e.g., Kikuchi and Takayabu 2004). In this study, we want to propose a new diagnostic framework. By using the GMS and its relevant quantities, we can systematically diagnose the convective amplification mechanism which includes various complicated factors.

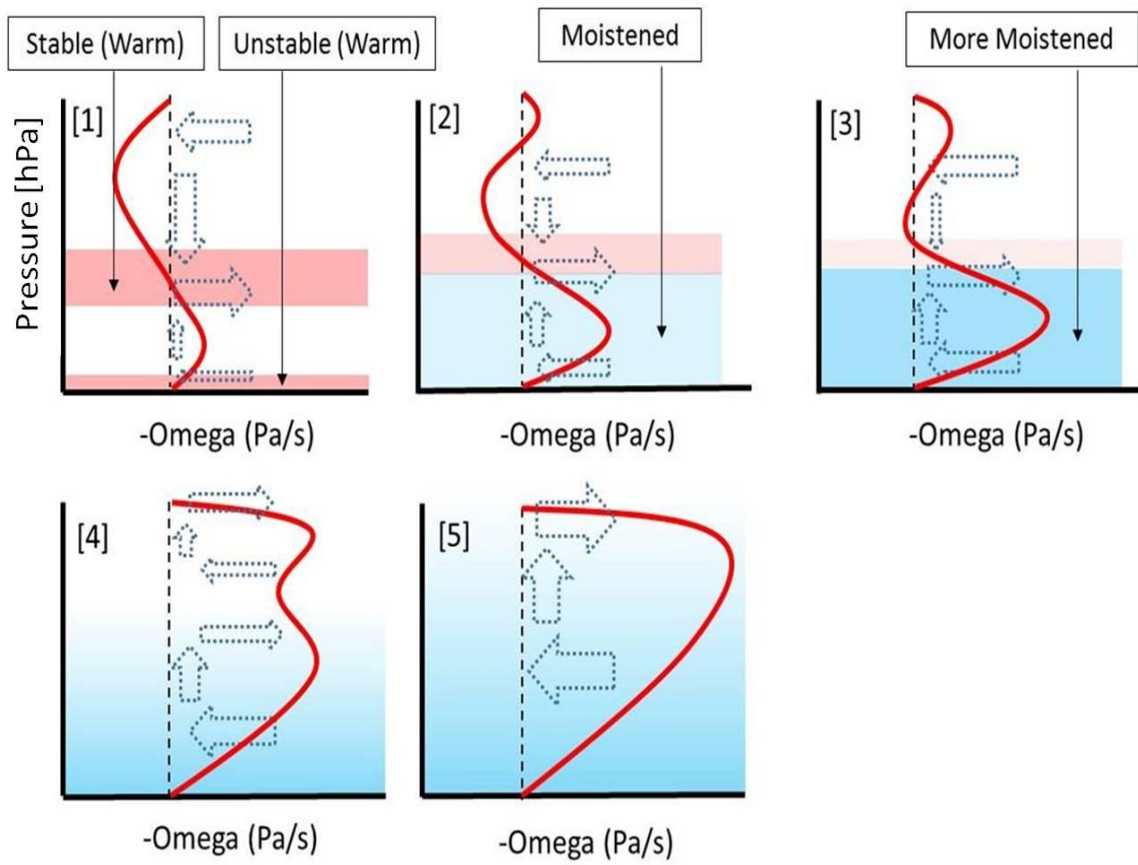


Figure 19: Schematic figure illustrating relation between temperature inversion, omega profile, moisture convergence, and convective amplification.

8. Future work

In this thesis we used simple running mean filters, but it would be more desirable to use Lanczos filter to remove the short time-scale variability. The main reason that we have to apply some time filter in this analysis is that we need to remove the tendency term from the DSE equation, Eq. (2). We claimed that most of the variances in the DSE tendency term are due to the diurnal cycle, so a time filter whose time window is longer than 24 hours is a necessary treatment for our analysis. This task can be done by the daily running mean filter. The main problem of the running mean filter is its shallow slope of the response function at the cut-off frequency. By using the 24-hour running mean filter, we actually removed not only the diurnal cycle, but also as much as 60% of the signals with 2 day periodicity. Based on the previous studies, we know there exist 2-day wave (equatorial inertia-gravity wave) signals in the TOGA COARE data. By using the running mean, we lost 60% of the signals of 2-day waves. Therefore, we would like to reproduce all figures by using Lanczos filter instead of daily running mean.

We also need to clarify the physical interpretations of horizontal MSE advection. We claimed that it is approximately random with respect to the convective life-cycles on shorter time scales. We can verify that idea by plotting the same kind of figure as Fig. 13 by removing the horizontal advection from the definition of the GMS-criticality. If the horizontal advection is random with respect to the convective life-cycle, then we will get a similar result as Fig. 13 even after removing the horizontal advective term from the consideration.

There is another task which is easy to do, but very worthwhile doing. Recently, new field campaign data has been made publicly available, that is called DYNAMO. DYNAMO, which took place in the Indian Ocean, was conducted in the same way as TOGA COARE. The group of people who constructed the DYNAMO sounding data, the data construction methodology, and the data structure are the same as TOGA COARE, thus I can apply my programming scripts written for TOGA COARE to the DYNAMO data set very easily. We would like to test whether or not the conclusion we drew from the TOGA COARE analysis is true for the DYNAMO data.

9. References

- Andersen, J. A., and Z. Kuang, 2011: Moist Static Energy Budget of MJO-like Disturbances in the Atmosphere of a Zonally Symmetric Aquaplanet. *J. Climate*, **25**, 2782–2804.
- Back, L. E., and C. S. Bretherton, 2006: Geographic variability in the export of moist static energy and vertical motion profiles in the tropical Pacific. *Geophys. Res. Lett.*, **33**, L17810, doi:10.1029/2006GL026672.
- Benedict, J. J., and D. A. Randall, 2007: Observed Characteristics of the MJO Relative to Maximum Rainfall. *J. Atmos. Sci.*, **64**, 2332–2354.
- Bretherton, C. S., and P. K. Smolarkiewicz, 1989: Gravity Waves, Compensating Subsidence and Detrainment around Cumulus Clouds. *J. Atmos. Sci.*, **46**, 740–759.
- , M. E. Peters, and L. E. Back, 2004: Relationships between Water Vapor Path and Precipitation over the Tropical Oceans. *J. Climate*, **17**, 1517–1528
- Charney, J. G., 1963: A Note on Large-Scale Motions in the Tropics. *J. Atmos. Sci.*, **20**, 607–609.
- , 1969: A Further Note on Large-Scale Motions in the Tropics. *J. Atmos. Sci.*, **26**, 182–185.
- Duchon, C. E., 1979: Lanczos Filtering in One and Two Dimensions. *J. Appl. Meteor.*, **18**, 1016–1022.
- Fairall, C. W., E. F. Bradley, J. E. Hare, A. A. Grachev, and J. B. Edson, 2003: Bulk Parameterization of Air–Sea Fluxes: Updates and Verification for the COARE Algorithm. *J. Climate*, **16**, 571–591.
- Frierson, D. M. W., 2007: Convectively Coupled Kelvin Waves in an Idealized Moist General Circulation Model. *J. Atmos. Sci.*, **64**, 2076–2090.
- Gill, A. E., 1980: Some simple solutions for heat-induced tropical circulation. *Q.J.R. Meteorol. Soc.*, **106**, 447–462.
- Haertel, P. T., and G. N. Kiladis, 2004: Dynamics of 2-Day Equatorial Waves. *J. Atmos. Sci.*, **61**, 2707–2721.

- Hannah, W. M., and E. D. Maloney, 2014: The moist static energy budget in NCAR CAM5 hindcasts during DYNAMO. *J. Adv. Model. Earth Syst.* accepted.
- Johnson, R. H., T. M. Rickenbach, S. A. Rutledge, P. E. Ciesielski, and W. H. Schubert, 1999: Trimodal Characteristics of Tropical Convection. *J. Climate*, **12**.
- Kikuchi, K., and Y. N. Takayabu, 2004: The development of organized convection associated with the MJO during TOGA COARE IOP: Trimodal characteristics. *Geophys. Res. Lett.*, **31**, L10101, doi:10.1029/2004GL019601.
- Kiladis, G. N., M. C. Wheeler, P. T. Haertel, K. H. Straub, and P. E. Roundy, 2009: Convectively coupled equatorial waves. *Rev. Geophys.*, **47**, RG2003, doi:10.1029/2008RG000266.
- Mapes, B., S. Tulich, J. Lin, and P. Zuidema, 2006: The mesoscale convection life cycle: Building block or prototype for large-scale tropical waves? *Dynamics of Atmospheres and Oceans*, **42**, 3–29.
- Masunaga, H., 2012: Short-Term versus Climatological Relationship between Precipitation and Tropospheric Humidity. *J. Climate*, **25**, 7983–7990.
- Matsuno, T., 1966: Quasi-geostrophic motions in the equatorial area. *Journal of the Meteorological Society of Japan*, **44**, 25–42.
- Neelin, J. D., and I. M. Held, 1987: Modeling Tropical Convergence Based on the Moist Static Energy Budget. *Mon. Wea. Rev.*, **115**, 3–12.
- , and J.-Y. Yu, 1994: Modes of Tropical Variability under Convective Adjustment and the Madden–Julian Oscillation. Part I: Analytical Theory. *J. Atmos. Sci.*, **51**, 1876–1894.
- , O. Peters, and K. Hales, 2009: The Transition to Strong Convection. *J. Atmos. Sci.*, **66**.
- Peters, M. E., and C. S. Bretherton, 2006: Structure of tropical variability from a vertical mode perspective. *Theor. Comput. Fluid Dyn.*, **20**, 501–524.
- Pritchard, M. S., and C. S. Bretherton, 2013: Causal Evidence that Rotational Moisture Advection is Critical to the Superparameterized Madden–Julian Oscillation. *J. Atmos. Sci.*, **71**.
- Raymond, D. J., S. L. Sessions, A. H. Sobel, and Ž. Fuchs, 2009: The Mechanics of Gross Moist Stability. *J. Adv. Model. Earth Syst.*, **1**, 9.
- Sobel, A., and E. Maloney, 2012: An Idealized Semi-Empirical Framework for Modeling the Madden–Julian Oscillation. *J. Atmos. Sci.*, **69**, 1691–1705.

- , and ——, 2013: Moisture Modes and the Eastward Propagation of the MJO. *J. Atmos. Sci.*, **70**, 187–192.
- Sobel, A. H., and C. S. Bretherton, 2000: Modeling Tropical Precipitation in a Single Column. *J. Climate*, **13**, 4378–4392.
- Stephens, G. L., P. J. Webster, R. H. Johnson, R. Engelen, and T. L’Ecuyer, 2004: Observational Evidence for the Mutual Regulation of the Tropical Hydrological Cycle and Tropical Sea Surface Temperatures. *J. Climate*, **17**, 2213–2224.
- Sugiyama, M., 2009: The Moisture Mode in the Quasi-Equilibrium Tropical Circulation Model. Part I: Analysis Based on the Weak Temperature Gradient Approximation. *J. Atmos. Sci.*, **66**, 1507–1523.
- Takayabu, Y. N., K.-M. Lau, and C.-H. Sui, 1996: Observation of a Quasi-2-Day Wave during TOGA COARE. *Mon. Wea. Rev.*, **124**, 1892–1913.
- Tian, B., and V. Ramanathan, 2003: A Simple Moist Tropical Atmosphere Model: The Role of Cloud Radiative Forcing. *J. Climate*, **16**, 2086–2092.
- Velden, C. S., and J. A. Young, 1994: Satellite Observations during TOGA COARE: Large-Scale Descriptive Overview. *Mon. Wea. Rev.*, **122**, 2426–2441.
- Webster, P. J., and R. Lukas, 1992: TOGA COARE: The Coupled Ocean—Atmosphere Response Experiment. *Bull. Amer. Meteor. Soc.*, **73**, 1377–1416.
- Yanai, M., and R. H. Johnson, 1993: Impacts of Cumulus Convection on Thermodynamic Fields. *Metor. Monogr.*, **24**, 39–62.
- , S. Esbensen, and J.-H. Chu, 1973: Determination of Bulk Properties of Tropical Cloud Clusters from Large-Scale Heat and Moisture Budgets. *J. Atmos. Sci.*, **30**, 611–627.
- , B. Chen, and W. Tung, 2000: The Madden–Julian Oscillation Observed during the TOGA COARE IOP: Global View. *J. Atmos. Sci.*, **57**, 2374–2396.